International Journal of Earth Sciences
https://doi.org/10.1007/s00531-022-02171-8

ORIGINAL PAPER

# Composition and thermal evolution of the lithospheric mantle beneath the Ribeira Belt, SE Brazil: evidence from spinel peridotite xenoliths

Vidyã Vieira Almeida[1,2] · Valdecir de Assis Janasi[2] · Frederico Meira Faleiros[2] · Antonio Simonetti[3] · Renato Moraes[2]

Received: 12 May 2021 / Accepted: 2 February 2022


**Abstract**
This study reports the first geochemical and Pb isotopic data for mantle xenoliths from beneath the Neoproterozoic Ribeira Belt, southeastern Brazil. The cm-sized spinel peridotite xenoliths are hosted by a Cretaceous lamprophyre dike that intruded high-grade metamorphic rocks. Major- and trace-element compositions of the main minerals indicate that the xenoliths derive from a shallow fertile mantle that has undergone a low degree of melt extraction (2–9% partial melting). On the basis of modeled isochemical phase diagrams for lherzolites, pressure and temperature conditions are inferred to vary from 1300–1350 °C and 17–19 kbar (fertile composition) to 1330–1430 °C and 17–23 kbar (relatively depleted composition), which correspond to high geothermal gradients of 65–80 mW/m$^2$. Temperatures of last equilibration calculated based on the average REE content of pyroxenes for the same lherzolite samples vary from 1233 ± 56 °C to 1085 ± 42 °C, while conventional thermometry ($T_{BKN}$) yields average values of 807 and 755 °C, indicating re-equilibration at lower temperatures. Pb isotope ratios of clinopyroxene define a mixing line that intercepts the Stacey-Kramers two-stage terrestrial Pb evolution curve at ca. 200 Ma. Linear regressions yield two errorchrons of 56 ± 75 Ma and 571 ± 99 Ma (95% confidence level). These results combined with the ages and tectonic settings of host rocks are suggestive of an overprint of a younger tectono-thermal event, most likely related to the opening of the South Atlantic Ocean, over a mantle previously equilibrated during the Precambrian development of the Ribeira Belt.

**Keywords** Spinel peridotite · Mantle xenoliths · Melt extraction · Isochemical diagrams · Ribeira Belt

## Introduction

Investigations that focus on the composition and physical properties of the subcontinental lithospheric mantle (SCLM) have an impact on the geological models put forward for the evolution of cratons and orogenic belts, and on the nature of magmas associated with igneous provinces (e.g., Griffin et al. 2009; Vauchez et al. 2012; Pearson et al. 2014). The SCLM plays an active role in major tectonic events that affect the whole tectonic plates, and these can be recorded in mantle samples hosted in mantle-derived alkaline magmas (e.g., Tommasi and Vauchez 2015; Liu et al. 2019).

The properties of the SCLM beneath Brazil have been mainly constrained by previous geophysical and geochemical studies (e.g., Rocha et al. 2011; Assumpção et al. 2011; Bastow et al. 2015; Chmyz et al. 2019), and in lesser degree via the examination of the composition of mantle xenoliths from various tectonic settings. Most of these mantle xenoliths are hosted in either Cenozoic (52–7 Ma) alkali basalts (e.g., in the Borborema Province, NE Brazil, related to the Macau and Pico do Cabuji volcanic fields; Rivalenti et al. 2000; Liu et al. 2019; Ngonge et al. 2016, 2019), or in Permian–Triassic (270–240 Ma) to Cretaceous (120–80 Ma) kimberlite-like rocks (e.g., from north and central regions of Brazil that are located in the Amazonian and São Francisco cratons and adjacent orogenic belts; Heaman et al.

✉ Vidyã Vieira Almeida
vidya.almeida@cprm.gov.br

[1] Geological Survey of Brazil (CPRM), Geodynamics Division, Regional Superintendency for São Paulo, Rua Costa 55, São Paulo 01304-010, Brazil

[2] Department of Mineralogy and Geotectonics, Institute of Geosciences, University of São Paulo, Rua do Lago 562, São Paulo 05508-080, Brazil

[3] Department of Civil and Environmental Engineering and Earth Sciences, University of Notre Dame, Notre Dame, IN, USA

Published online: 18 February 2022

1998; Carlson et al. 2007; Costa et al. 2008; Kaminsky et al. 2010; Almeida et al. 2014; Felgate 2014). Old Re depletion model ages (average 2400 Ma) of these mantle xenoliths have provided evidence for multi-stage melt extraction from the mantle beneath the São Francisco Craton since Archean-Proterozoic times (e.g., Carlson et al. 2007), while initial $^{187}Os/^{188}Os$ of mantle xenoliths from the Borborema Province are similar to those of modern abyssal peridotites (Ngonge et al. 2019). Os model ages range from ~ 0 to 1700 Ma suggesting partial replacement of old lithospheric mantle by juvenile material, which was triggered by the opening of the Equatorial Atlantic Ocean (Ngonge et al. 2019; Liu et al. 2019). These combined evidence attest for a complex evolution of the subcontinental lithosphere throughout the Brazilian territory as a result of the multiple tectono-thermal events through geologic time.

The Ribeira Belt (Fig. 1a), located in southeast Brazil, is a Neoproterozoic orogen developed during the assembly of West Gondwana as part of the Mantiqueira Province (Brito Neves et al. 1999; Faleiros et al. 2011). The orogen consists of several distinct tectonic terranes with Proterozoic supracrustal rocks (Statherian-to-Cambrian; 1760–540 Ma) and local exposures of gneiss–migmatite basement of Paleoproterozoic age (2200–1750 Ma) (Siga Junior 1995; Cury et al. 2002; Heilbron et al. 2004, 2017; Campanha et al. 2008, 2015, 2016, 2019; Henrique-Pinto et al. 2015; Ricardo et al. 2020). These rocks are intruded by voluminous Late Neoproterozoic to Cambrian granitic magmatism (620–540 Ma; e.g., Janasi et al. 2001; Meira et al. 2015; Heilbron et al. 2020) and sectioned by a large-scale transcurrent shear zone system.

The evolution of the orogen starts with a precollisional stage (860–620 Ma) followed by three tectono metamorphic episodes that are related to the accretion of the inner continental magmatic arc (620–595 Ma), accretion of intraoceanic magmatic arcs (595–565 Ma), and collision of the Cabo Frio Terrane (535–510 Ma) (Heilbron and Valeriano 2020). Lower Cretaceous (~ 134–130 Ma) magmatism of the Paraná Magmatic Province, related to the breakup of Gondwana and opening of the South Atlantic Ocean, occurs as massive dike swarms of tholeiitic affinity and alkaline–carbonatite complexes (e.g., Raposo 2017; Almeida et al. 2018). A second main episode of alkaline magmatism occurred at ~ 85 Ma, with late manifestations as young as ~ 55 Ma. The relationship of the Mesozoic magmatism with mantle plumes is still contentious (e.g., Heron 2018; Cheng et al. 2020; Beccaluva et al. 2019) as there are other processes that can lead to mantle melting (e.g., thermal insulation in supercontinents; Coltice et al. 2009).

The age(s) of the SCLM and its role in subsequent magmatism is a key piece to understand the geological evolution of the whole Mantiqueira Province, helping to reconstruct robust geological and geophysical models. In particular, given that it has experienced major tectonic events that include collision of terranes (Faleiros et al. 2011) and rifting (e.g., Lamotte et al. 2015), direct study of this SCLM and its

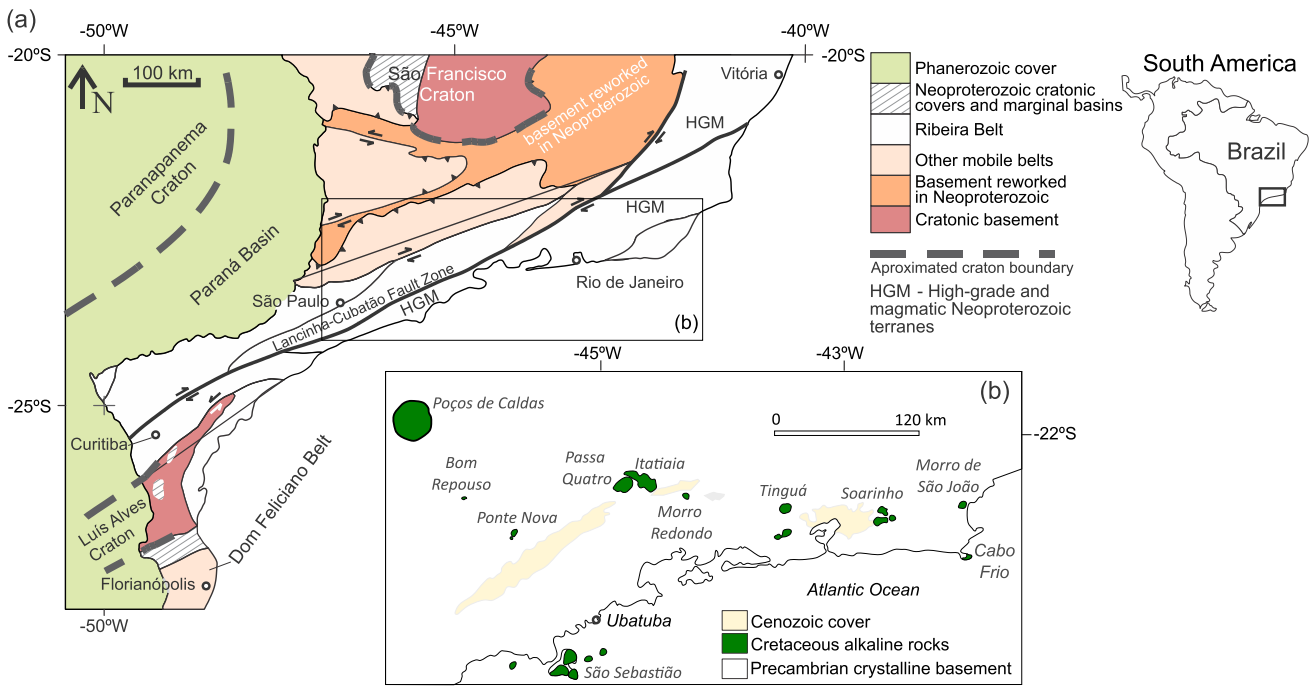


**Fig. 1** Regional geological context of southeastern Brazil. **a** Simplified geological map of the Ribeira Belt. Modified from Faleiros et al. (2016). **b** Simplified map of the plutonic complexes from the Serra do Mar region with the location of Ubatuba. Adapted from Azzone et al. (2016)

space–time evolution would benefit enormously from direct sampling. However, occurrences of mantle xenoliths within the Ribeira Belt area are scarce, and in essence restricted to those described in this work.

In this context, the present work aims to investigate the nature of the upper mantle beneath the Ribeira Belt through the description and analyses of spinel-facies peridotite xenoliths hosted by a lamprophyre dike that outcrops at Vermelha Beach, Ubatuba City, São Paulo State. We present compositional data for the main minerals (major and trace elements) obtained via electron microprobe and LA-ICP-MS analyses, and in situ Pb isotope measurements in clinopyroxene. These data allow us to constrain the age of the events that affected the SCLM, and perform isochemical phase diagram modeling and quantification of pressure and temperature conditions of last equilibration and thus contribute to the understanding of mantle evolution during Precambrian orogenic events, and Cretaceous magmatic events related with breakup of Pangea and opening and evolution of the South Atlantic Ocean.

## Geological setting

The Mesozoic magmatism in south-southeast of Brazil comprises the Lower Cretaceous (~ 134 Ma) tholeiitic occurrences of the Paraná-Etendeka Magmatic Province (PEMP), including voluminous flood basalts, sills, and dike swarms (Ponta Grossa, Serra do Mar and Florianópolis). In addition, there are Lower and Upper Cretaceous alkaline intrusions that include plutonic complexes and dikes, both generated during two main magmatic episodes: the first contemporaneous with the tholeiitic magmatism (~ 130 Ma) and the second peaking at ~ 85 Ma, with some occurrences as young as ~ 55 Ma (e.g., Gomes et al. 2011; Janasi et al. 2011; Almeida et al. 2018).

The lamprophyre dikes from Vermelha Beach, Ubatuba, are part of the Cretaceous ENE-trending Serra do Mar dike swarm (SMDS) that outcrop along the coastline of São Paulo state. Several alkaline complexes (e.g., Ponte Nova, Ilha de São Sebastião, Fig. 1b) dominated by syenites and nepheline syenites, with lesser amounts of gabbros, carbonatites, and ultramafic rocks intrude Precambrian metamorphic terranes of the Ribeira Belt in this region (Brotzu et al. 2005). The intrusions are structurally related to ENE–EW faults zones generated in the Neoproterozoic Brasiliano-Pan African Cycle (e.g., Faleiros et al. 2011). The latter were reactivated in the Cretaceous due to extensional movements related to the opening of the South Atlantic Ocean; the second episode is possibly associated with a regional uplifting caused by the Trindade plume (Thompson et al. 1998); however, these hypotheses lack an overall consensus.

Garda (1995), Garda et al. (1995), Brotzu et al. (2005), and Raposo (2017) presented detailed description of the dikes from the region. These are concentrated between the cities of São Sebastião and Ubatuba and crosscut Proterozoic poly-metamorphic rocks of the Costeiro Complex (Garda 1995; Raposo 2017). The tholeiitic dikes vary from basalt to dacite, while the alkaline rocks include a suite of silica undersaturated rocks (foidite, basanite, and phonolite) and lamprophyres (Brotzu et al. 2005; Vicentini et al. 2015; Raposo 2017). The age of the dike swarm is still contentious, as lamprophyres from the area seem related to the Upper Cretaceous magmatism responsible for the formation of the major alkaline intrusions of the area (Bellieni et al. 1990; Raposo 2017). A $^{40}Ar/^{39}Ar$ age of 85.4 ± 0.4 Ma was recently obtained for biotite from a tephriphonolite dike (Azzone et al. 2018). The tholeiitic occurrences are related to the Lower Cretaceous magmatism of the PEMP, as constrained by $^{40}Ar/^{39}Ar$ ages (130 Ma; Deckart et al. 1998; Regelous 1993).

### The host lamprophyre dike

The spinel peridotite mantle xenoliths are located at the core of a subvertical 1.5 m-thick dike of a dark-gray kaersutite lamprophyre (Fig. 2a–c) that shows significant zoning between the core and an aphanitic rim. In some places, the core presents ellipsoidal contours that locally form a breccia (Fig. 2d) and are interpreted as a volcanic conduit (Garda et al. 1995). These portions bear xenoliths of the country rock (a foliated charnockite) and mantle xenoliths in a fine-grained spherulitic vitreous matrix. In thin section, the lamprophyre shows olivine phenocrysts/xenocrysts immersed in a matrix composed of brownish clinopyroxene (Ti-augite), kaersutite, olivine, biotite, feldspathoids, and Fe–Ti oxides. The whole-rock composition classifies the rock as a basanite with 40 wt% of $SiO_2$, 3 wt% of $TiO_2$, 12 wt% MgO, 1.8 wt% of $Na_2O$, and 1.7 wt% $K_2O$.

## Analytical techniques

Major elements in minerals were analyzed in a JEOL JXA-8600 electron microprobe at the NAP-Geoanalitica, Institute of Geosciences, University of São Paulo. Analyses were performed at 15 kV acceleration voltage and 20 nA beam current; beam diameter was normally 5 µm. Standards were natural and synthetic minerals; standards used in pyroxene analyses include wollastonite (Si, Ca), rutile (Ti), anorthite (Al), $Cr_2O_3$ (Cr), diopside (Mg), olivine (Mn, Fe), natural Ba silicate (Ba), albite (Na), and asbesto (K). Corrections were performed using the PROZA procedure (Bastin et al. 1984). Trace-element analyses in clinopyroxene, orthopyroxene, and olivine were performed by LA-Q-ICP-MS at

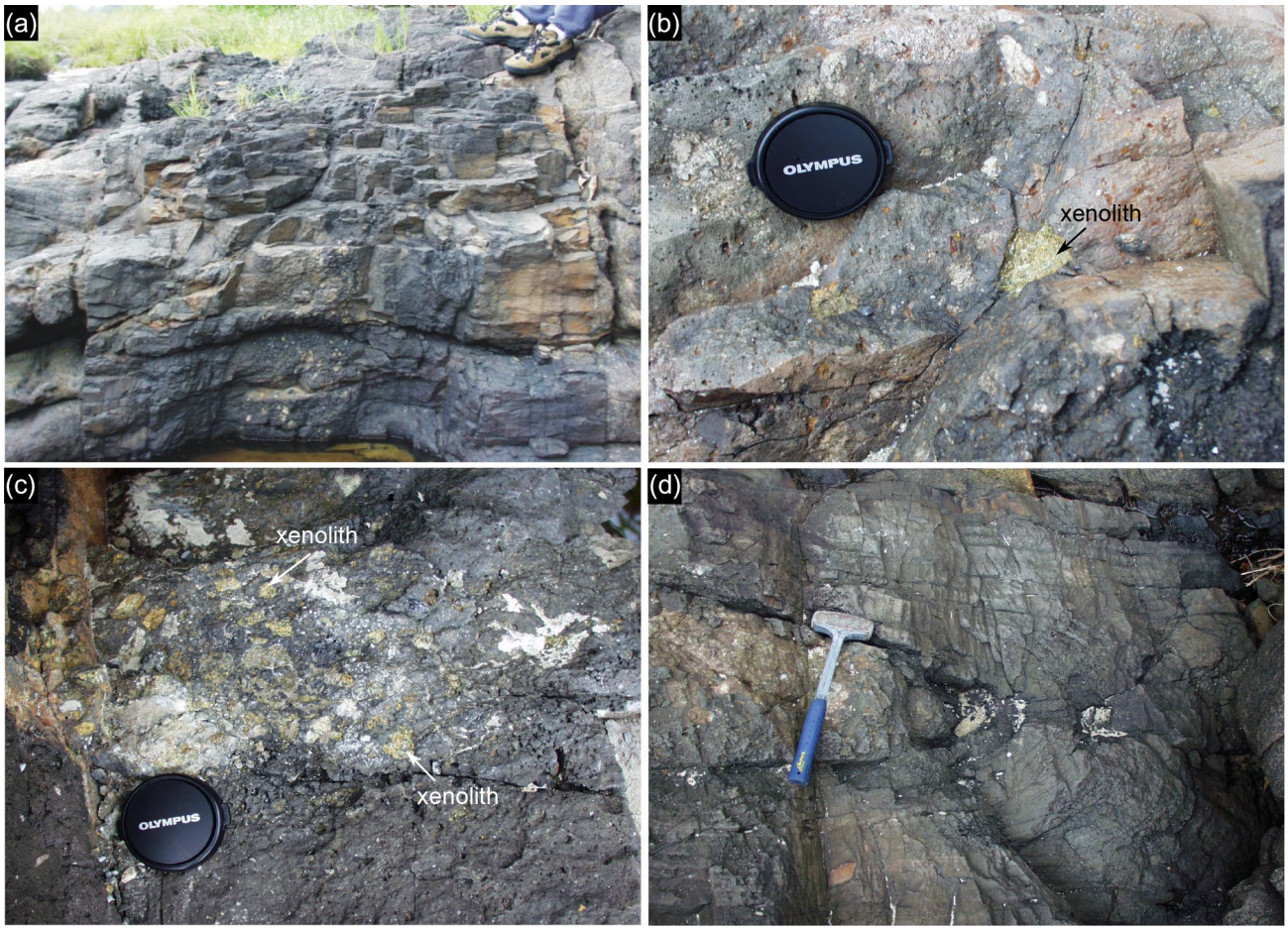


**Fig. 2** **a** Kaesurtite lamprophyre dike that hosts the mantle xenoliths. **b** Mantle xenoliths (yellowish green) enclosed in the lamprophyre. **c** Concentration of mantle xenoliths (yellowish green) in the dike. **d** Ellipsoidal contours at the center of the dike

NAP-Geoanalitica, using a Parkin-Elmer ELAN-600 quadrupole ICP-MS with a 216 nm Nd-YAG New-Wave laser ablation system, with a spatial resolution of 20–40 µm. The average detection limits of the LA-Q-ICP-MS and the average compositions obtained for the calibration standards (NIST 610 and NIST 612 glasses) and quality controls (BCR and BHVO) are in the supplementary material. The concentration of Ca from the electron microprobe analyses was used as internal standard for clinopyroxene analyses. The concentration of Mg was used as internal standard for orthopyroxene and olivine analyses. The data reduction was performed using the Glitter software (Griffin et al. 2008). Detailed information about the analytical procedure at the LA-Q-ICP-MS laboratory can be found in Andrade et al. (2014).

*P–T* isochemical phase diagrams were constructed for bulk compositions representative of spinel lherzolite samples XM-3 and XM-1 using the Perple_X software (Connolly 2005), version 6.8.7, and the internally consistent thermodynamic database of Holland and Powell (2011) (tc-ds622, hp622ver.dat in Perple_X). The modeled bulk compositions are indicated in Table 1 and were determined by combining quantitative modal and chemical mineral data. Uncertainties about the positions of assemblage field boundaries associated with point-counted mineral proportions that propagate in an individual phase diagram are quantified to be ± 50 °C and ± 1 kbar

**Table 1** Bulk compositions used in phase diagram modeling

| Sample | XM-3 | XM-1 |
|---|---|---|
| $SiO_2$ | 44.07 | 42.18 |
| $Al_2O_3$ | 5.78 | 1.19 |
| $Cr_2O_3$ | 0.60 | 0.30 |
| FeO | 8.25 | 8.41 |
| MgO | 37.55 | 44.50 |
| CaO | 2.79 | 2.50 |
| $Na_2O$ | 0.24 | 0.14 |
| $O_2$ | 0.08 | 0.02 |

(2σ) for a 20% degree of modal proportion uncertainty (Palin et al. 2016). The diagrams were calculated in the $Na_2O$–CaO–FeO–MgO–$Al_2O_3$–$SiO_2$–$O_2$–$Cr_2O_3$ (NCFMASOCr) model system. The $Fe_2O_3$ contents in the modeled bulk compositions, expressed by the appropriate $O_2$ contents to correct to FeO, were estimated based on charge balance in the chemical formulas of the minerals. Estimated $Fe_2O_3$ contents vary from 0.3 to 0.16 wt%, which agree with $Fe_2O_3$ contents in the range of 0.1–0.4 wt% measured in peridotite xenoliths by $^{57}$Fe Mössbauer spectroscopy (Canil et al. 1994). The solution models for clinopyroxene, orthopyroxene, olivine, spinel, garnet, plagioclase, and silicate melt are from Jennings and Holland (2015).

The temperature estimates are based on the REE content of the pyroxenes and the Fe–Mg exchange between the pyroxenes (Brey and Koehler 1990), and these were calculated using the excel spreadsheet available in Liang et al. (2013). The temperature estimates based on the composition of clinopyroxene of Mercier (1980) were obtained using software PTQuick (Simakov and Dolivo-Dobrovolsky 2009).

The Pb isotope compositions of individual clinopyroxene grains were obtained using petrographic thin sections at the MITERAC ICP-MS Facility, University of Notre Dame (USA). In situ Pb isotope ratios were obtained using an NWR193 nm laser ablation system coupled to a Nu Plasma II MC-ICP-MS instrument. Individual clinopyroxene grains were analyzed in raster mode using a 150 µm spot size, repetition rate of between 7 and 12 Hz, and an energy density of 10–12 J/cm$^3$. Prior to lasering of clinopyroxene grains, a 45 s on peak blank measurement was conducted and followed by a 60 s laser ablation interval. The raw Pb isotope data were measured and calculated using the Nu Instruments TRA (Time-Resolved-Analysis) software. Unknown analyses from each of the samples were bracketed by analysis ($n = 4$ measurements) of the NIST SRM 614 glass standard to correct for instrumental drift and mass bias. As described in Chen and Simonetti (2015) and Smart et al. (2017), the instrumental mass bias was corrected by adopting the exponential law and the Pb isotope values for NIST SRM 614 (Baker et al. 2004). On the basis of repeated measurements ($n = 10$) of the NIST SRM 614 standard, the average external reproducibility (2σ level) for the $^{208}$Pb/$^{204}$Pb, $^{207}$Pb/$^{204}$Pb, $^{206}$Pb/$^{204}$Pb, $^{207}$Pb/$^{206}$Pb, and $^{208}$Pb/$^{206}$Pb ratios are ± 0.14, 0.059, 0.066, 0.0015, and 0.003, respectively.

## Spinel-facies mantle xenoliths

The spinel peridotite samples are subrounded, medium- to coarse-grained xenoliths and are up to 2 cm in diameter. The larger samples were classified based on mineral counting and visual estimates and all correspond to peridotites (lherzolite and wehrlite, Table 2) with 0.6 to 8 vol% of spinel. The sample XM-3 presents high proportion of orthopyroxene (> 30 vol%). The detailed study was performed in five representative xenoliths and some xenocrysts.

The spinel lherzolite samples show protogranular texture, with minerals showing both linear and embayed contacts (Fig. 3a–c). The samples display up to 4 mm-sized, anhedral, partially altered olivine grains with slight undulose extinction. Brownish orthopyroxene is ~ 1.5 mm size and shows microfractures and fine exsolution lamellae concentrated in the core of the grains. Light green clinopyroxene is ~ 2 mm size and contains fluid inclusions trails. Brownish and olive-green spinel is included in orthopyroxene or involves partially clinopyroxene grains. Tiny sulfide crystals are present as accessory phases.

A wehrlite xenolith contains partially serpentinized olivine, clinopyroxene, and minor orthopyroxene with straight and curved contacts forming a protogranular texture. A reaction rim is present at the contact with the host rock, composed of euhedral clinopyroxene, opaque minerals, and small olivine grains. The sample also shows a region with a symplectic intergrowth of clinopyroxene and olivine (Fig. 3d).

Small xenoliths (< 1 cm) and xenocrysts of olivine and orthopyroxene were also studied and typically show reaction rims with the host lamprophyre (Fig. 3e). Orthopyroxene xenocrysts may have exsolution lamellae similar to those shown by grains from the bigger xenoliths (Fig. 3f).

**Table 2** Classification of the bigger mantle xenoliths

| Sample | Texture | Ol | Opx | Cpx | Sp | Opc | Classification |
|---|---|---|---|---|---|---|---|
| XM-1* | Protogranular | 81.8 | 6.7 | 10.7 | 0.6 | 0.2 | Spinel lherzolite |
| XM-2 | Protogranular with symplectite | 72 | 3 | 25 | – | – | Wehrlite |
| XM-3* | Protogranular | 49.4 | 34.7 | 11.8 | 3.5 | 0.6 | Spinel lherzolite |
| XM-9 h | Protogranular | 66 | 10 | 15 | 8 | 1 | Spinel lherzolite |

*Point counting

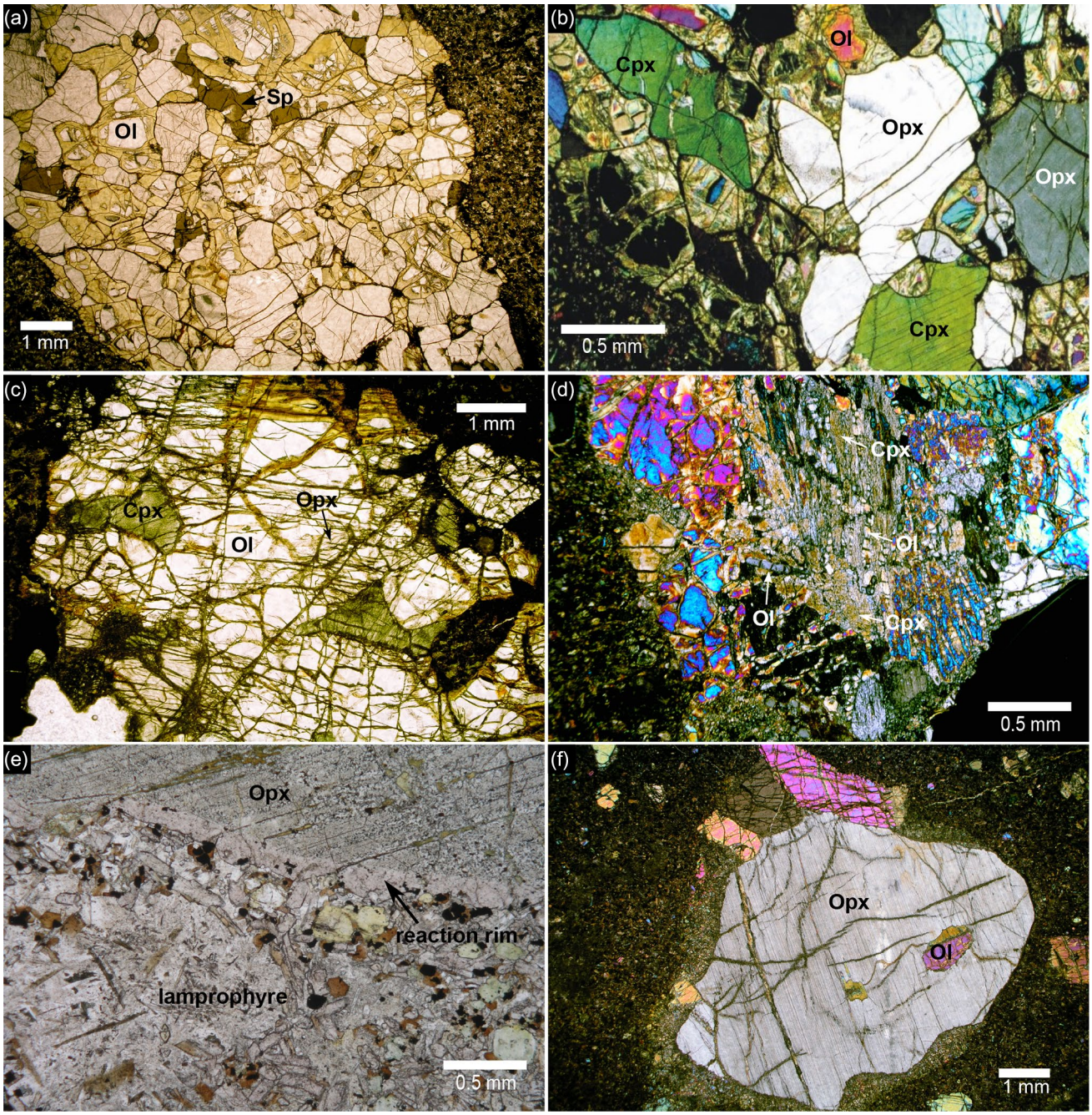


**Fig. 3** Photomicrographs of the mantle xenoliths. **a** Texture of sample XM-3 showing minerals with straight and curved contacts with spinel (Sp) and olivine (Ol). **b** Detailed view of the sample XM-3, with clinopyroxene (Cpx), orthopyroxene (Opx), and olivine. **c** Texture of sample XM-1 showing clinopyroxene, olivine, and orthopyroxene. **d** Wehrlite showing a symplectic intergrowth between clinopyroxene and olivine. **e** Reaction rim between mantle xenolith and the host lamprophyre. **f** Orthopyroxene xenocryst with exsolution lamellae

## Mineral chemistry

### Major elements

Representative major-element analyses of olivine, pyroxene, and spinel are listed in Tables 3 and 4 and as supplementary material.

Olivine has high Mg# (100*Mg/(Mg + Fe)), which is typical of mantle xenoliths (88–91), with slight differences among the three xenolith samples; olivine from sample XM-1 has the highest Mg# (90.5–90.8), XM-2 the lowest (88.2–89.4), while XM-3 has intermediate values (89.4–89.6). Olivine from two smaller fragments was also analyzed, and those from XM-9h overlap XM-3, while

**Table 3** Representative major-element compositions of olivine (Ol) and spinel (Sp) of the mantle xenoliths

| Sample | XM-9 g | XM-9 h | XM-1 | XM-2 | XM-3 | Sample | XM-9 h | XM-9 h | XM-3 | XM-3 | XM-3 | XM-1 |
|---|---|---|---|---|---|---|---|---|---|---|---|---|
| Mineral | Ol | Ol | Ol | Ol | Ol | Mineral | Sp | Sp | Sp | Sp | Sp | Sp |
| Position | Rim | Core | Core | Core | Core | Position | Core | Core | Core | Core | Rim | Rim |
| $SiO_2$ | 39.92 | 39.96 | 40.20 | 40.55 | 40.08 | $TiO_2$ | 0.13 | 0.08 | 0.06 | 0.08 | 0.05 | 0.10 |
| $TiO_2$ | 0.00 | 0.03 | 0.00 | 0.02 | 0.00 | $Al_2O_3$ | 58.00 | 57.70 | 58.75 | 59.37 | 60.62 | 49.56 |
| $Al_2O_3$ | 0.00 | 0.00 | 0.00 | 0.01 | 0.00 | $Cr_2O_3$ | 9.33 | 9.69 | 7.52 | 6.53 | 6.16 | 14.94 |
| FeO | 9.25 | 10.15 | 9.31 | 11.16 | 10.32 | FeO | 10.57 | 10.96 | 9.95 | 9.85 | 10.81 | 9.49 |
| MnO | 0.18 | 0.14 | 0.14 | 0.21 | 0.18 | $Fe_2O_3$* | 2.02 | 1.60 | 2.71 | 2.61 | 1.38 | 5.43 |
| MgO | 50.88 | 49.91 | 49.65 | 48.15 | 48.86 | MnO | 0.09 | 0.09 | 0.08 | 0.10 | 0.05 | 0.14 |
| CaO | 0.02 | 0.02 | 0.02 | 0.03 | 0.01 | MgO | 20.01 | 19.61 | 20.24 | 20.23 | 19.88 | 19.51 |
| $Na_2O$ | 0.01 | 0.00 | 0.02 | 0.00 | 0.00 | ZnO | 0.22 | 0.18 | 0.25 | 0.23 | 0.18 | 0.13 |
| $K_2O$ | 0.01 | 0.00 | 0.00 | 0.00 | 0.00 | | | | | | | |
| $Cr_2O_3$ | 0.00 | 0.03 | 0.03 | 0.04 | 0.00 | | | | | | | |
| NiO | 0.40 | 0.36 | 0.39 | 0.31 | 0.40 | | | | | | | |
| Total | 100.65 | 100.58 | 99.76 | 100.48 | 99.86 | Total | 100.38 | 99.91 | 99.56 | 98.99 | 99.14 | 99.32 |
| Si | 0.974 | 0.979 | 0.988 | 0.996 | 0.989 | FeOI | 12.39 | 12.397 | 12.388 | 12.194 | 12.056 | 14.375 |
| Al | 0.000 | 0.000 | 0.000 | 0.000 | 0.000 | Al | 1.763 | 1.764 | 1.789 | 1.811 | 1.842 | 1.568 |
| Ti | 0.000 | 0.001 | 0.000 | 0.000 | 0.000 | Ti | 0.003 | 0.002 | 0.001 | 0.001 | 0.001 | 0.002 |
| $Fe^{2+}$ | 0.189 | 0.208 | 0.191 | 0.229 | 0.213 | Cr | 0.190 | 0.199 | 0.154 | 0.134 | 0.126 | 0.317 |
| Mn | 0.004 | 0.003 | 0.003 | 0.004 | 0.004 | Fe2 | 0.228 | 0.238 | 0.215 | 0.213 | 0.233 | 0.213 |
| Mg | 1.851 | 1.822 | 1.820 | 1.764 | 1.797 | Fe3 | 0.039 | 0.031 | 0.053 | 0.051 | 0.027 | 0.110 |
| Ca | 0.000 | 0.001 | 0.001 | 0.001 | 0.000 | Mn | 0.002 | 0.002 | 0.002 | 0.002 | 0.001 | 0.003 |
| Na | 0.001 | 0.000 | 0.001 | 0.000 | 0.000 | Mg | 0.770 | 0.759 | 0.780 | 0.781 | 0.765 | 0.781 |
| K | 0.000 | 0.000 | 0.000 | 0.000 | 0.000 | Zn | 0.000 | 0.000 | 0.000 | 0.000 | 0.000 | 0.000 |
| Ni | 0.008 | 0.007 | 0.008 | 0.006 | 0.008 | | | | | | | |
| Total | 3.027 | 3.021 | 3.012 | 3.000 | 3.011 | Total | 2.995 | 2.995 | 2.994 | 2.993 | 2.995 | 2.994 |
| Mg# | 91.0 | 90.0 | 91.0 | 89.0 | 89.0 | Cr# | 9.7 | 9.7 | 7.9 | 6.9 | 6.4 | 16.8 |

*$Fe^{2+}/Fe^{3+}$ ratios estimated using Carmichael (1967) procedure for spinel

olivines from XM-9g encompass the whole spectrum of Mg#. Apart from $SiO_2$, abundances for other major oxides are very low; NiO varies from 0.25 to 0.4 wt%; typically, the lower contents (< 0.32 wt%) are present in the xenolith with lower Mg# (XM-2). The rims of the grains located adjacent to the contact between the xenolith and the host rock show slightly lower Mg# (86).

Orthopyroxene from all samples shows a very small range of Mg# (89.5–91). The difference between xenoliths XM-1 and XM-3 parallels the variation shown by coexisting olivine, with orthopyroxene from XM-1 showing systematically higher Mg# (90.4–90.6) and no overlap (XM-3 Opx Mg# = 89.5–90.0). Orthopyroxene from xenolith XM-2 has Mg# in the same range for those from XM-3, but Al contents are much lower. A positive correlation between Al total and $TiO_2$ abundances is noted among the xenoliths, with XM-3 showing the highest contents and XM-2 (in which $TiO_2$ is close to zero) the lowest (Fig. 4a).

Clinopyroxene Mg# varies from 90.0 to 91.7, except in reaction rims at the contact with the host lamprophyre (Mg# = 83). The CaO content of clinopyroxene varies from 19.2 to 23.0 wt%, while $Na_2O$ varies from 0.6 to 2.3 wt%. Figure 4b compares Mg# and Al total of coexisting clinopyroxene and orthopyroxene. The Mg# of clinopyroxene is always slightly higher than the Mg# of orthopyroxene, and Al total are similar in pyroxenes from XM-1 and XM-2 with the latter showing the lowest contents (Fig. 4c). The compositions for clinopyroxene from both sample XM-3 and XM-9h again overlap in Fig. 4c and have the highest Al total contents. Al content of pyroxene from mantle peridotite is indicative of the degree of fertility, and this confirms that samples XM-3 and 9h are the most fertile from the sample set.

Most Al in clinopyroxene corresponds to the jadeite component and is corroborated by the positive correlation between Al (IV) and Na contents (Fig. 4d). Clinopyroxene from host lamprophyre is optically distinct with brownish tint typical of Ti-augite and has higher Ti and $Fe^{3+}$ contents (Table 4). Clinopyroxene from the spinel lherzolites XM-3 and XM-9h shows cores with higher concentrations of $Al_2O_3$ (6.2–7.6 wt%), $TiO_2$ (0.5–0.8 wt%), and $Na_2O$ (1.8–2.3 wt%).

**Table 4** Representative major-element compositions of orthopyroxene (Opx) and clinopyroxene (Cpx) of the mantle xenoliths

| Sample | XM-9 g | XM-9 h | XM-2 | XM-1 | XM-3 | XM-9 h | XM-9 h | XM-1 | XM-2 | XM-2 | XM-3 | XM-3 | Lamp |
|---|---|---|---|---|---|---|---|---|---|---|---|---|---|
| Mineral | Opx | Opx | Opx | Opx | Opx | Cpx | Cpx | Cpx | Cpx | Cpx | Cpx | Cpx | Cpx |
| Position | Core | Core | Rim | Core | Core | Core | Rim | Core | Core | rim | Core | rim | Core |
| $SiO_2$ | 54.86 | 55.82 | 57.37 | 55.50 | 55.12 | 52.06 | 51.72 | 52.09 | 53.67 | 53.18 | 51.59 | 51.72 | 40.11 |
| $TiO_2$ | 0.03 | 0.19 | 0.00 | 0.09 | 0.16 | 0.60 | 0.68 | 0.22 | 0.04 | 0.16 | 0.60 | 0.59 | 5.54 |
| $Al_2O_3$ | 3.59 | 4.15 | 1.65 | 3.98 | 4.52 | 7.48 | 7.46 | 4.39 | 1.49 | 1.75 | 7.36 | 6.68 | 9.91 |
| FeO | 5.88 | 6.49 | 7.02 | 6.18 | 6.83 | 2.55 | 2.60 | 2.49 | 2.96 | 3.07 | 2.58 | 2.50 | 8.14 |
| MnO | 0.14 | 0.16 | 0.22 | 0.19 | 0.15 | 0.10 | 0.10 | 0.04 | 0.08 | 0.13 | 0.05 | 0.07 | 0.09 |
| MgO | 34.08 | 33.72 | 33.39 | 33.03 | 33.01 | 13.99 | 13.85 | 15.39 | 17.68 | 17.41 | 13.56 | 14.18 | 10.80 |
| CaO | 1.01 | 0.33 | 0.60 | 0.38 | 0.24 | 19.74 | 20.36 | 22.05 | 22.10 | 22.31 | 21.76 | 21.86 | 23.43 |
| $Na_2O$ | 0.06 | 0.07 | 0.35 | 0.04 | 0.01 | 2.29 | 2.17 | 1.23 | 0.58 | 0.59 | 1.86 | 1.67 | 0.45 |
| $K_2O$ | 0.00 | 0.00 | 0.14 | 0.00 | 0.00 | 0.01 | 0.00 | 0.01 | 0.01 | 0.00 | 0.00 | 0.01 | 0.01 |
| $Cr_2O_3$ | 0.70 | 0.28 | 0.16 | 0.44 | 0.29 | 1.40 | 0.82 | 0.79 | 0.41 | 0.53 | 0.70 | 0.54 | 0.07 |
| Total | 100.33 | 101.21 | 100.90 | 99.83 | 100.33 | 100.21 | 99.75 | 98.68 | 99.01 | 99.12 | 100.05 | 99.82 | 98.56 |
| TSi | 1.881 | 1.902 | 1.965 | 1.920 | 1.899 | 1.875 | 1.871 | 1.910 | 1.961 | 1.944 | 1.866 | 1.874 | 1.528 |
| TAl | 0.119 | 0.098 | 0.035 | 0.080 | 0.101 | 0.125 | 0.129 | 0.090 | 0.039 | 0.056 | 0.134 | 0.126 | 0.445 |
| TFe3 | 0.000 | 0.000 | 0.000 | 0.000 | 0.000 | 0.000 | 0.000 | 0.000 | 0.000 | 0.000 | 0.000 | 0.000 | 0.027 |
| M1Al | 0.025 | 0.069 | 0.031 | 0.082 | 0.082 | 0.192 | 0.189 | 0.099 | 0.025 | 0.019 | 0.180 | 0.159 | 0.000 |
| M1Ti | 0.001 | 0.005 | 0.000 | 0.002 | 0.004 | 0.016 | 0.018 | 0.006 | 0.001 | 0.004 | 0.016 | 0.016 | 0.159 |
| M1Fe3 | 0.077 | 0.016 | 0.028 | 0.000 | 0.003 | 0.021 | 0.032 | 0.044 | 0.042 | 0.055 | 0.032 | 0.037 | 0.185 |
| M1Fe2 | 0.000 | 0.000 | 0.000 | 0.000 | 0.000 | 0.000 | 0.000 | 0.000 | 0.000 | 0.000 | 0.022 | 0.007 | 0.041 |
| M1Cr | 0.019 | 0.008 | 0.004 | 0.012 | 0.008 | 0.040 | 0.023 | 0.023 | 0.012 | 0.015 | 0.020 | 0.015 | 0.002 |
| M1Mg | 0.878 | 0.903 | 0.936 | 0.904 | 0.903 | 0.732 | 0.738 | 0.829 | 0.921 | 0.907 | 0.731 | 0.766 | 0.613 |
| M1Ni | 0.000 | 0.000 | 0.000 | 0.000 | 0.000 | 0.000 | 0.000 | 0.000 | 0.000 | 0.000 | 0.000 | 0.000 | 0.000 |
| M2Mg | 0.864 | 0.810 | 0.769 | 0.799 | 0.792 | 0.019 | 0.009 | 0.013 | 0.042 | 0.042 | 0.000 | 0.000 | 0.000 |
| M2Fe2 | 0.092 | 0.169 | 0.173 | 0.179 | 0.194 | 0.056 | 0.047 | 0.033 | 0.049 | 0.039 | 0.025 | 0.032 | 0.007 |
| M2Mn | 0.004 | 0.005 | 0.006 | 0.006 | 0.004 | 0.003 | 0.003 | 0.001 | 0.002 | 0.004 | 0.001 | 0.002 | 0.003 |
| M2Ca | 0.037 | 0.012 | 0.022 | 0.014 | 0.009 | 0.762 | 0.789 | 0.866 | 0.865 | 0.874 | 0.843 | 0.849 | 0.957 |
| M2Na | 0.004 | 0.004 | 0.024 | 0.002 | 0.001 | 0.160 | 0.152 | 0.087 | 0.041 | 0.042 | 0.131 | 0.117 | 0.033 |
| M2K | 0.000 | 0.000 | 0.006 | 0.000 | 0.000 | 0.000 | 0.000 | 0.000 | 0.000 | 0.000 | 0.000 | 0.000 | 0.001 |
| Wo | 1.90 | 0.63 | 1.15 | 0.75 | 0.47 | 47.83 | 48.79 | 48.52 | 45.03 | 45.51 | 50.98 | 50.14 | 52.205 |
| En | 89.26 | 89.48 | 88.13 | 89.56 | 88.97 | 47.16 | 46.18 | 47.13 | 50.14 | 49.40 | 44.20 | 45.26 | 33.479 |
| Fs | 8.84 | 9.90 | 10.72 | 9.69 | 10.56 | 5.01 | 5.04 | 4.35 | 4.83 | 5.10 | 4.82 | 4.60 | 14.316 |
| Mg# | 91.16 | 90.25 | 89.45 | 90.49 | 89.59 | 90.7 | 90.44 | 91.62 | 91.37 | 90.99 | 90.25 | 90.97 | 70.22 |

Lamp—lamprophyre

Spinel is present in the more fertile samples XM-3 and 9h and is characterized by Cr# = 6–10 and Mg# = 74–75. Spinel from xenolith XM-1 has higher Cr# and lower Mg# (Fig. 5a).

## Trace elements

Results of trace-element analyses by LA-ICP-MS of olivine and pyroxene are presented in Table 5. Olivine has negligible contents of incompatible elements. Ni is the most abundant trace element at 3200–3300 ppm in both samples XM-1 and XM-3; Ni concentrations drop to ~ 2500 ppm in XM-2. In contrast, olivine from XM-2 contains higher Zn (120 ppm) and Mn (1900 ppm) contents relative to the other two samples. Olivine from XM-3 is distinguished by higher Ti (~ 30 vs. 4–5 ppm in XM-1 and XM-2) and lower Cr (< 8 vs. 22–25 ppm) contents. Significant contents of P (56–74 ppm) are present in all analyzed crystals.

Orthopyroxene has low REE contents with sample XM-3 showing higher Y compared to XM-1 (0.7–0.9 vs. 0.3 ppm), which is paralleled by the HREE. Similarly to olivine, orthopyroxene from XM-3 is distinct from that of XM-1 by its higher Ti (1000–1100 vs. ~ 400 ppm) and lower Cr (2100–2400 vs. ~ 3000 ppm) abundances. Overall, clinopyroxene is host to most of the incompatible elements for the xenolith samples. Chondrite-normalized REE patterns for three xenolith samples are markedly contrasted. Clinopyroxene from XM-3 has a flat pattern with

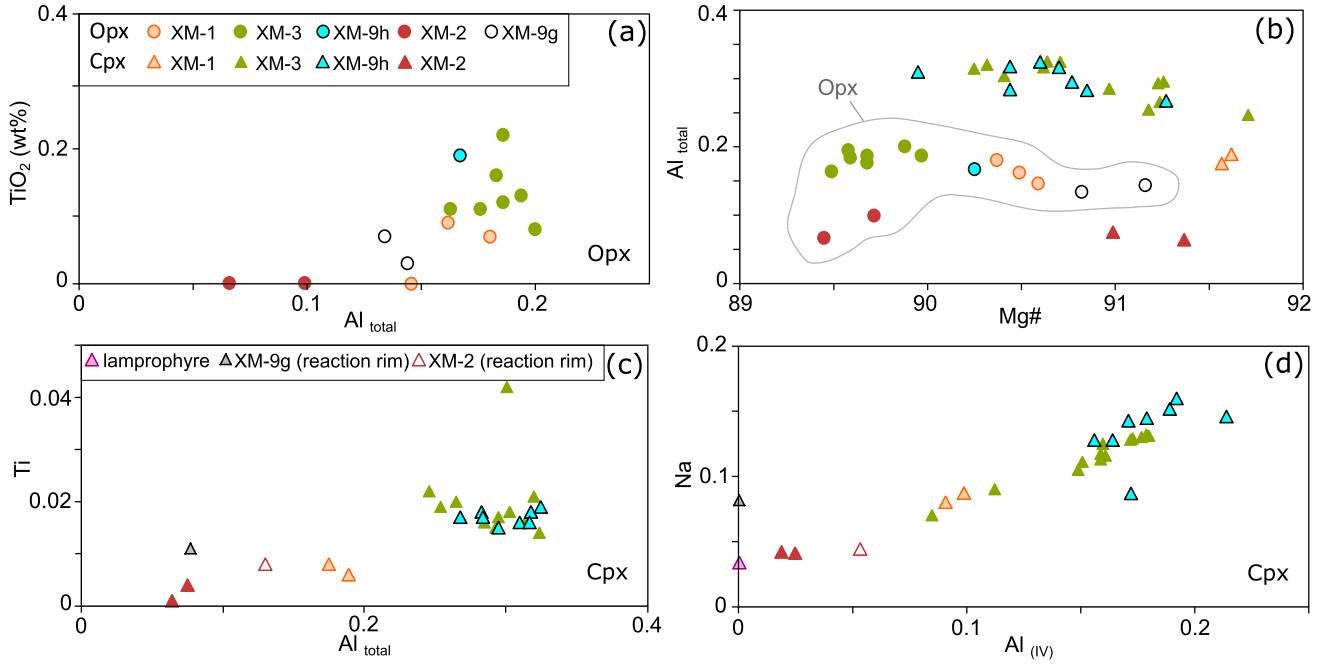


**Fig. 4** **a** $Al_{total}$ vs. $TiO_2$ (wt%) of orthopyroxene (Opx) of the xenolith samples. **b** Mg# vs. $Al_{total}$ with a comparison between orthopyroxene and clinopyroxene (Cpx) compositions. **c** $Al_{total}$ vs. Ti of clinopyroxene. **d** Positive correlation between $Al_{(IV)}$ and Na of clinopyroxene of the xenolith samples

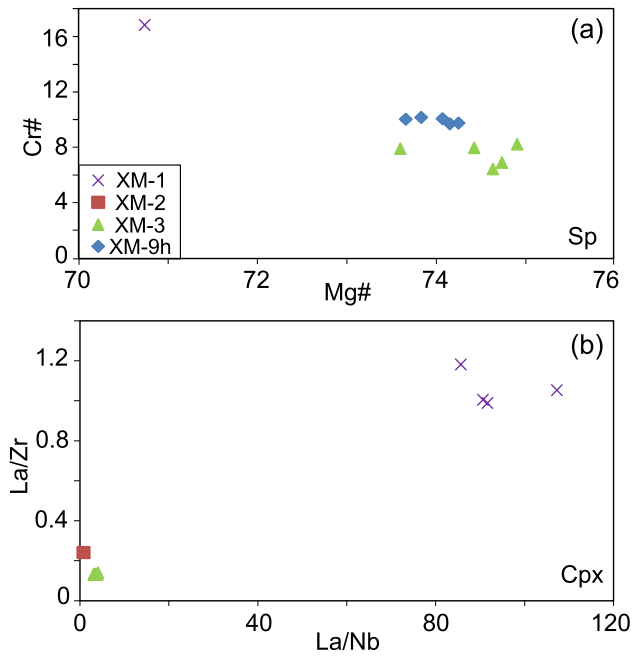


**Fig. 5** **a** Mg# vs. Cr# diagram with the composition of spinel in the xenolith samples. **b** LILE/HFS (La/Nb, La/Zr) ratios of clinopyroxenes of the samples XM-1, XM-2 and XM-3

$(La/Yb)_N = 0.6–1$ and concentrations at ten times chondrite (Fig. 6a). Clinopyroxene from XM-1 exhibits a flat pattern for the REEs heavier than Gd ($(Gd/Lu)_N = 0.8—1.4$) at low concentrations (average 6 × chondrite), and a pronounced enrichment of the LREEs, attaining ~ 100 × chondrite for La (Fig. 6a). Clinopyroxene from sample XM-2 shows an overall enrichment of all REEs with a maximum at Nd that results in a concave-up shape for the LREEs ($(La/Nd)_N < 1$). The distribution coefficients of the REE between clinopyroxene and orthopyroxene (Dcpx/opx), calculated with the average compositions, and a diagram showing the Dcpx/opx for two xenoliths (XM-1 and XM-3) in comparison with the Dcpx/opx of Hellebrand et al. (2005) are in the supplementary material. The two samples (XM-1 and XM-3) show similar Dcpx/opx for most of the REE.

Primitive mantle-normalized multi-element plots illustrate important contrasts in the behavior of incompatible elements in clinopyroxene from the studied xenoliths. Clinopyroxene from sample XM-3 shows slightly negative Zr + Hf anomalies ($(Sm/Zr)_N$ from 1.8 to 3.2) and depletion of LILE and Nb (Fig. 6b). LILE/HFS ratios for the clinopyroxene from sample XM-1 are systematically higher as observed in Figs. 5b and 6b. It also exhibits well-defined negative anomalies of HFSEs (Ti, Zr, Hf, and Nb), which are especially highlighted by the relatively high contents of LREEs, Th, U, and Ba. Clinopyroxene from XM-2 contrast with that of XM-1 by overall higher contents of incompatible elements (except U, Th, and Pb), but especially by higher abundances of Nb and Ta and a pronounced negative Ti anomaly (Fig. 6b).

**Table 5** Representative trace element compositions of olivine (Ol), orthopyroxene (Opx), and clinopyroxene (Cpx) of the mantle xenoliths. Concentrations are in ppm

| Sample | XM-1 | XM-2 | XM-3 | XM-3 | XM-1 | XM-1 | XM-1 | XM-1 | XM-2 | XM-3 | XM-3 | XM-3 |
|---|---|---|---|---|---|---|---|---|---|---|---|---|
| Mineral | Ol | Ol | Ol | Opx | Opx | Opx | Cpx | Cpx | Cpx | Cpx | Cpx | Cpx |
| P | 67.62 | 57.15 | 66.79 | 55.76 | 30.40 | 50.66 | 44.38 | 84.70 | < dl | 86.22 | 76.88 | 45.45 |
| Sc | 1.45 | 1.57 | 2.54 | 15.97 | 13.50 | 14.67 | 68.04 | 65.46 | 43.25 | 58.76 | 53.50 | 60.23 |
| Ti | 3.89 | 4.99 | 35.41 | 975.67 | 364.80 | 422.58 | 1242.17 | 962.90 | 1007.49 | 6065.27 | 4842.49 | 5259.36 |
| Cr | 24.59 | 21.78 | < dl | 2272.02 | 2923.96 | 3016.29 | 8261.51 | 7502.41 | 3940.09 | 5614.71 | 5027.44 | 5206.18 |
| Mn | 1110.18 | 1886.87 | 1094.72 | 1173.95 | 1139.93 | 1121.64 | 588.40 | 588.31 | 1245.55 | 745.24 | 684.60 | 687.88 |
| Co | 160.95 | 148.28 | 159.89 | 57.76 | 57.06 | 55.76 | 25.89 | 20.45 | 31.79 | 18.76 | 18.46 | 19.29 |
| Ni | 3335.45 | 2483.52 | 3283.64 | 649.85 | 632.18 | 642.36 | 383.09 | 338.22 | 475.64 | 307.16 | 268.31 | 281.20 |
| Cu | 0.68 | 0.45 | < dl | < dl | 0.32 | 0.76 | 0.50 | 0.54 | 4.28 | 1.01 | 0.48 | 0.99 |
| Zn | 42.79 | 120.45 | 32.57 | 23.38 | 31.55 | 26.52 | 29.55 | 10.38 | 34.08 | 6.54 | 5.12 | 7.01 |
| Ga | < dl | < dl | 0.15 | 3.74 | 3.19 | 3.18 | 3.85 | 2.62 | 12.69 | 5.50 | 4.25 | 4.75 |
| Rb | < dl | < dl | < dl | < dl | < dl | < dl | 0.21 | 0.12 | 19.39 | 0.16 | < dl | < dl |
| Sr | < dl | < dl | < dl | < dl | 1.19 | 0.26 | 265.39 | 189.23 | 634.33 | 93.85 | 78.39 | 81.29 |
| Y | 0.02 | 0.10 | < dl | 0.68 | 0.27 | 0.35 | 8.53 | 8.29 | 50.71 | 18.24 | 17.28 | 18.02 |
| Zr | 0.01 | < dl | < dl | 0.66 | 0.61 | 0.65 | 19.01 | 16.53 | 74.95 | 21.27 | 17.89 | 19.09 |
| Nb | 0.02 | < dl | < dl | < dl | < dl | 0.00 | 0.26 | 0.16 | 17.61 | 0.85 | 0.60 | 0.81 |
| Sn | 1.15 | < dl | 1.77 | < dl | 0.66 | 0.69 | 0.90 | 1.13 | 2.03 | < dl | < dl | 1.55 |
| Ba | 0.03 | 0.06 | < dl | 0.22 | 0.70 | 0.06 | 81.24 | 43.41 | 25.36 | < dl | 0.20 | < dl |
| La | < dl | < dl | < dl | 0.01 | 0.10 | 0.03 | 22.46 | 17.38 | 17.62 | 2.84 | 2.34 | 2.52 |
| Ce | < dl | 0.02 | 0.01 | < dl | 0.20 | 0.03 | 32.63 | 28.41 | 80.30 | 9.28 | 7.60 | 7.50 |
| Pr | < dl | < dl | < dl | < dl | < dl | < dl | 2.54 | 2.37 | 14.33 | 1.53 | 1.12 | 0.98 |
| Nd | < dl | < dl | 0.07 | < dl | 0.09 | < dl | 7.00 | 8.57 | 79.23 | 7.49 | 6.18 | 5.50 |
| Sm | < dl | < dl | 0.05 | < dl | < dl | 0.02 | 1.12 | 1.30 | 18.70 | 2.51 | 1.27 | 1.73 |
| Eu | < dl | < dl | 0.08 | < dl | < dl | < dl | 0.46 | 0.50 | 6.09 | 0.90 | 0.73 | 0.65 |
| Gd | < dl | < dl | 0.07 | < dl | < dl | 0.02 | 1.46 | 1.15 | 14.76 | 2.73 | 2.64 | 2.99 |
| Tb | < dl | < dl | 0.02 | 0.01 | 0.01 | < dl | 0.22 | 0.25 | 2.41 | 0.42 | 0.40 | 0.59 |
| Dy | < dl | 0.02 | < dl | 0.12 | 0.05 | 0.05 | 1.34 | 1.29 | 12.73 | 4.43 | 2.61 | 3.14 |
| Ho | < dl | < dl | 0.03 | 0.05 | 0.02 | 0.02 | 0.40 | 0.33 | 1.92 | 0.84 | 0.58 | 0.77 |
| Er | < dl | < dl | < dl | 0.07 | 0.06 | 0.04 | 0.98 | 0.87 | 4.23 | 2.19 | 1.75 | 1.71 |
| Tm | < dl | < dl | < dl | < dl | 0.01 | 0.01 | 0.20 | 0.16 | 0.55 | 0.37 | 0.30 | 0.25 |
| Yb | < dl | < dl | 0.06 | 0.19 | 0.21 | 0.11 | 1.03 | 1.27 | 3.90 | 2.82 | 2.25 | 1.47 |
| Lu | 0.00 | 0.01 | < dl | 0.09 | 0.01 | 0.03 | 0.13 | 0.11 | 0.35 | 0.27 | 0.29 | 0.37 |
| Hf | < dl | 0.04 | 0.06 | < dl | 0.02 | < dl | 0.39 | 0.45 | 0.87 | 0.43 | 0.62 | 0.38 |
| Ta | 0.00 | < dl | < dl | < dl | 0.00 | < dl | < dl | 0.01 | 0.33 | 0.16 | 0.11 | 0.03 |
| Pb | < dl | < dl | < dl | < dl | < dl | < dl | 2.90 | 2.46 | 0.82 | 0.49 | 0.19 | 0.17 |
| Th | < dl | 0.04 | < dl | < dl | 0.12 | 0.08 | 3.44 | 2.42 | 0.35 | 0.14 | 0.09 | 0.05 |
| U | 0.06 | < dl | < dl | 0.03 | 0.11 | 0.06 | 0.91 | 0.78 | < dl | < dl | 0.02 | < dl |

< dl—below detection limit

## Pb isotopes

The Pb isotope compositions for minerals characterized by very low U/Pb ratios reflect those predominantly inherited initially from the medium they last equilibrated with, and may therefore provide important age information (e.g., Hunt et al. 2012). In mantle samples, clinopyroxene has been the most feasible mineral for this kind of study due to its low U/Pb ratios and high closure temperatures for Pb diffusion during thermal events (e.g., Cherniak 1998; Jacob and Foley 1999; Schmidberger et al. 2007; Tappe et al. 2011; Hunt et al. 2012; Smart et al. 2014, 2017). This combination yields reliable age information and insights into the chemical nature of the SCLM. There are several previous works in which Pb isotope compositions of clinopyroxene proved to be fundamental in constraining the role of the mantle relative to major tectono-thermal events (e.g., collision of terranes, subduction, regional magmatism) of a given area (e.g.,

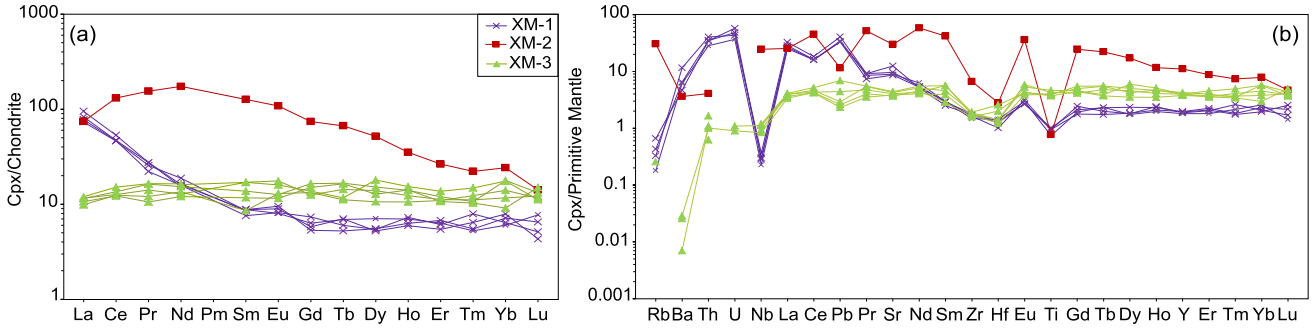


**Fig. 6** **a** Chondrite-normalized (McDonough and Sun 1995) REE patterns. **b** Primitive mantle-normalized (Sun and McDonough 1989) incompatible elements patterns of clinopyroxene of the mantle xenoliths

Slave Craton; Smart et al. 2014, 2017). Pb isotope compositions of clinopyroxene also help to identify open-system or mixing behavior, such as mantle metasomatism and host magma–mantle xenolith interaction (e.g., Smart et al. 2017).

Clinopyroxene from spinel lherzolite XM-1 has the highest Pb, U, and Th concentrations (2.4–3 ppm, 0.8–1.2 ppm, and 2.4–3.4 ppm, respectively) among the peridotite samples investigated here, and was therefore selected for in situ Pb isotope investigation by LA-MC-ICP-MS. Pb isotope ratios are presented in Table 6 and shown in Fig. 7. The Pb isotope compositions display considerable variation with $^{206}Pb/^{204}Pb$, $^{207}Pb/^{204}Pb$, and $^{208}Pb/^{204}Pb$ ratios that define the following ranges: 18.4–20.1, 15.6–17, and 38.7–41.8, respectively. The $^{206}Pb/^{204}Pb$ and $^{207}Pb/^{204}Pb$ ratios form a linear array (Fig. 7a) and intercept the Stacey-Kramers two-stage terrestrial evolution curve at ca. 200 Ma. The data reported here plot close to the isotopic field of Group I kimberlites (Smith 1983), and to the Pb isotopic composition of the host lamprophyre alkaline dike (Garda 1995) and alkaline dikes from the Serra do Mar region (Ponte Nova massif; Azzone et al. 2020). In a $^{238}U/^{204}Pb$ vs. $^{206}Pb/^{204}Pb$ isochron diagram (Fig. 7b), the results define two linear regressions that yield errorchron ages of $56 \pm 75$ Ma and $571 \pm 99$ Ma (95% confidence level). Given the large uncertainty associated with the former, it represents a younger event with no geological meaning.

## Pressure and temperature calculations

### Temperature calculations

The average composition of pyroxene from samples XM-1 and XM-3 was used for obtaining temperature calculations based on the REE geothermometer of Liang et al. (2013). The regression lines yield temperatures of last equilibration of $1031 \pm 47$ °C (XM-1) and $1136 \pm 37$ °C (XM-3) based on all of the REE data (Fig. 8a, b). However, the temperatures are $1085 \pm 42$ °C (XM-1) and $1233 \pm 56$ °C (XM-3) when excluding outlier elements from the linear regressions (Y,

**Table 6** Pb isotope analyses of clinopyroxene from sample XM-1

| Point | $^{206}Pb/^{204}Pb$ | 2σ | $^{207}Pb/^{204}Pb$ | 2σ | $^{208}Pb/^{204}Pb$ | 2σ | $^{207}Pb/^{206}Pb$ | 2σ | $^{208}Pb/^{206}Pb$ | 2σ |
|---|---|---|---|---|---|---|---|---|---|---|
| 1 | 18.40 | 0.19 | 15.62 | 0.16 | 38.66 | 0.42 | 0.8487 | 0.0009 | 2.1015 | 0.0023 |
| 2 | 18.64 | 0.14 | 15.83 | 0.12 | 39.22 | 0.31 | 0.8494 | 0.0009 | 2.1036 | 0.0011 |
| 3 | 18.77 | 0.22 | 15.99 | 0.18 | 39.62 | 0.43 | 0.8519 | 0.0013 | 2.1049 | 0.0022 |
| 4 | 18.76 | 0.16 | 15.94 | 0.13 | 39.56 | 0.33 | 0.8474 | 0.0012 | 2.1022 | 0.0021 |
| 5 | 18.50 | 0.24 | 15.68 | 0.20 | 38.88 | 0.51 | 0.8475 | 0.0010 | 2.1008 | 0.0010 |
| 6 | 18.52 | 0.19 | 15.76 | 0.16 | 38.95 | 0.40 | 0.8506 | 0.0011 | 2.1037 | 0.0018 |
| 7 | 18.47 | 0.17 | 15.69 | 0.15 | 38.99 | 0.38 | 0.8495 | 0.0011 | 2.1109 | 0.0019 |
| 8 | 18.49 | 0.13 | 15.66 | 0.10 | 39.08 | 0.31 | 0.8469 | 0.0016 | 2.1086 | 0.0021 |
| 9 | 19.49 | 0.12 | 16.55 | 0.11 | 41.07 | 0.23 | 0.8503 | 0.0009 | 2.1090 | 0.0019 |
| 10 | 19.27 | 0.13 | 16.41 | 0.11 | 40.68 | 0.29 | 0.8516 | 0.0011 | 2.1124 | 0.0025 |
| 11 | 19.31 | 0.13 | 16.36 | 0.11 | 40.59 | 0.25 | 0.8478 | 0.0009 | 2.1036 | 0.0027 |
| 12 | 20.11 | 0.25 | 17.09 | 0.22 | 42.17 | 0.54 | 0.8476 | 0.0010 | 2.0979 | 0.0021 |
| 13 | 19.89 | 0.21 | 16.88 | 0.18 | 41.83 | 0.45 | 0.8486 | 0.0007 | 2.1029 | 0.0021 |
| 14 | 18.91 | 0.19 | 16.10 | 0.16 | 39.91 | 0.38 | 0.8515 | 0.0010 | 2.1111 | 0.0020 |

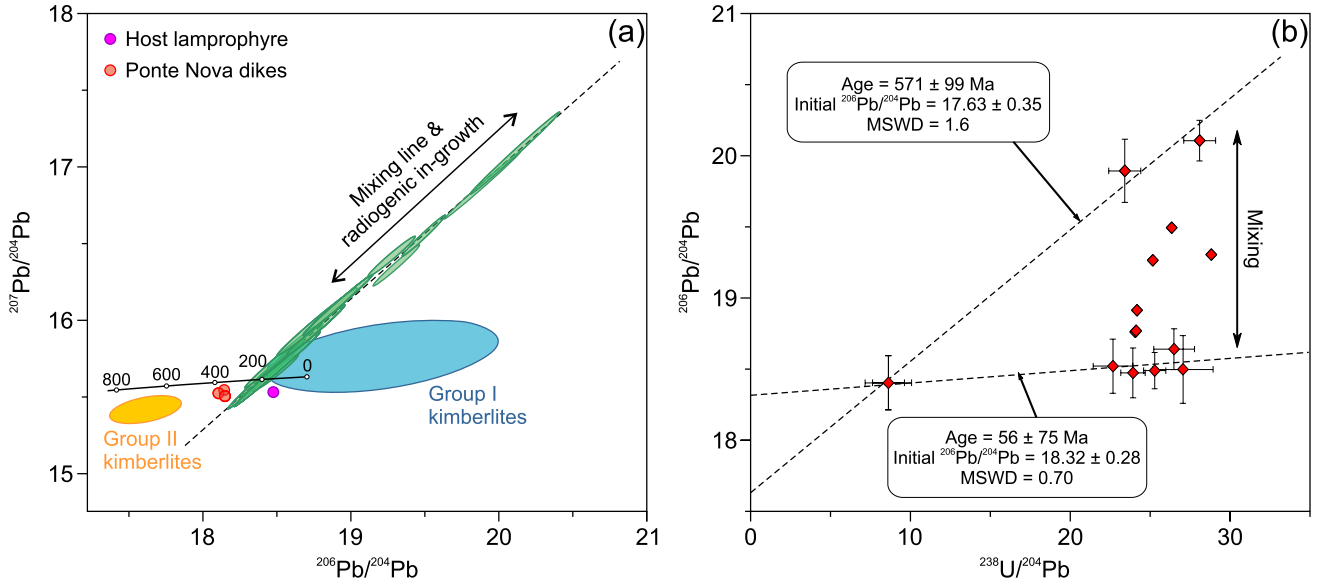


**Fig. 7** **a** Pb isotope compositions of clinopyroxene for sample XM-1. All ellipses represent a single analysis with the 2σ error. Two-stage terrestrial Pb growth curve from Stacey and Kramers (1975) (model ages are in Ma). Given the recent and young age of the metasomatic activity responsible for the addition of U, and the relatively low $^{238}U/^{204}Pb$ ratios of the pyroxenes, the initial Pb ratios would plot within the associated 2σ level uncertainties. The Pb isotopic composition of the host lamprophyre dike is from Garda (1995) ($^{206}Pb/^{204}Pb_i$ and $^{207}Pb/^{204}Pb_i$ are 18.476 and 15.530, respectively, calculated to 89 Ma), while the Pb isotopic composition of the alkaline dikes from the Serra do Mar region (Ponte Nova massif) is from Azzone et al. (2020) (the range of $^{206}Pb/^{204}Pb_i$ and $^{207}Pb/^{204}Pb_i$ ratios are 18.106–18.150 and 15.505–15.544, respectively, calculated to 87.6 Ma). **b** $^{238}U/^{204}Pb$ vs. $^{206}Pb/^{204}Pb$ isochron diagram showing the two errorchron ages for the clinopyroxene from sample XM-1

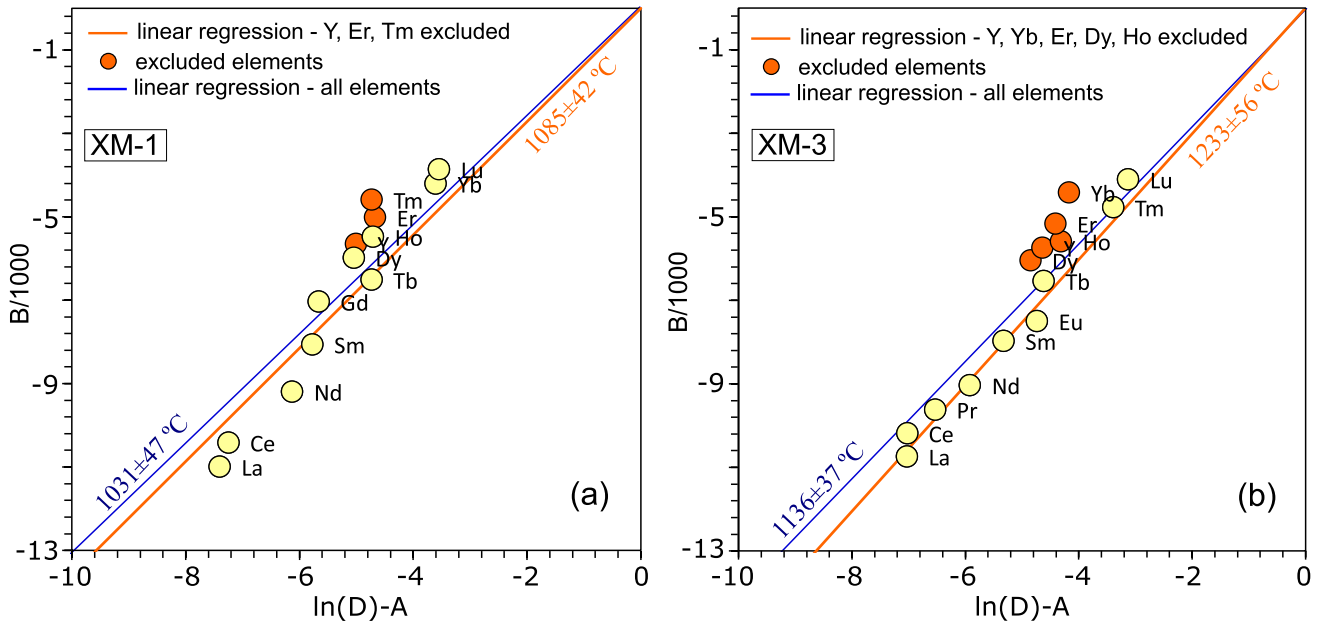


**Fig. 8** Linear regressions and temperatures derived from the REE-in-two-pyroxene thermometer ($T_{REE}$; Liang et al., 2013) for XM-1 (**a**) and XM-3 (**b**) samples. A, B are coefficients that represent functions of pyroxene composition and ionic radius of an element and D is the orthopyroxene–clinopyroxene partition coefficient for a trace element (Liang et al., 2013)

Er, Tm for XM-1 and Y, Yb, Er, Dy, Ho for XM-3; Fig. 8a, b). The latter values were considered the best calculations for the temperatures of last equilibration for both samples.

The average composition for the cores of the pyroxenes provided temperatures of last equilibration of 755 °C (XM-1) and 807 °C (XM-3) using the $T_{BKN}$ geothermometer of Brey and Koehler (1990), assuming a pressure of 20 and 18 kbar, respectively, based on the average results of the isochemical diagrams. The single clinopyroxene geothermometer of Mercier (1980) provided higher temperatures of 895 °C (XM-1) and 850 °C (XM-3) using the average composition of clinopyroxene. The average temperature of last equilibration of 928 ± 159 °C, 1055 ± 178 °C, and 759 ± 246 °C was also obtained, respectively, for samples XM-1, XM-3, and XM-9h by multiequilibria thermometry using THERMOCALC v. 326 (Powell and Holland 1994). THERMOCALC produced temperature conditions with large uncertainties, related with the version used, as the activity-composition models for mantle rocks were developed after v. 326 and were not implemented for newer versions in the average *P–T* mode.

### Isochemical phase diagrams

In the *P–T* phase diagram calculated for sample XM-3 (more fertile composition), the observed mineral assemblage containing clinopyroxene, orthopyroxene, olivine, and spinel is stable at 8–23 kbar and up to 1180–1440 °C when clinopyroxene is consumed in a partial melting reaction (Fig. 9a). The phase diagram was countered with compositional isopleths of Cr# and Fe (apfu) contents in spinel, Mg# contents in olivine and clinopyroxene and Al (apfu) contents in orthopyroxene (Fig. 9b, c). The measured compositions (Mg# in olivine = 90, Fe (apfu) in spinel = 0.25–0.26, Cr# in spinel = 0.80–0.90, Al (apfu) in orthopyroxene = 0.18) reasonably intersect at 1300–1350 °C and 17–19 kbar that corresponds to a geothermal gradient between 70 and 80 mW/m$^2$ using the geotherms of Hasterok and Chapman (2011) (Fig. 9d). Calculated modal isopleths indicate that 0.023–5 vol% of melt could be in equilibrium with the solid phases at these conditions (Fig. 9d).

In the *P–T* phase diagram modeled for sample XM-1 (relatively depleted composition), the equilibria fields for spinel lherzolites are for the most part similar to those calculated for the most fertile composition (Fig. 10a). Significant differences are restriction of stability fields for the assemblages Cpx–Opx–Ol–Grt and Opx–Ol–Spl–Liq, and a large expansion of the stability field for the assemblage Cpx–Ol–Grt–Spl (Fig. 10a; mineral abbreviations from Whitney and Means 2010), although with very low contents of spinel (0.1–0.3 vol.%) for pressures above 18 kbar. The phase diagram was countered with compositional isopleths of Mg# in olivine, Cr# in clinopyroxene and Fe (apfu) in spinel (Fig. 10b) and contents of Al (apfu) in orthopyroxene and Cr# in spinel (Fig. 10c). The measured compositions of Mg# in olivine, Al in orthopyroxene (0.16–0.17 apfu) and Cr# in clinopyroxene (0.11–0.12) intersect at 1300–1500 °C and 22–28 kbar (Fig. 10d) that corresponds to an approximate geothermal gradient between 65 and 75 mW/m$^2$ using the geotherms of Hasterok and Chapman (2011). Calculated modal isopleths indicate that up to 3 vol.% of melt could be in equilibrium with the solid phases at these conditions. The measured compositions of spinel were not reproduced in the modeled phase diagram.

## Discussion

### Heterogeneous partial melting and melt extraction: evidence from trace elements

The major- and trace-element compositions for olivine and pyroxene in textural equilibrium show considerable variation that can be related to different degrees of depletion of basaltic components (e.g., Ca, Al, Na, and Fe) due to partial melting and melt extraction (e.g., Norman et al. 1998). The higher $Al_2O_3$ content and nearly flat REE pattern of clinopyroxene and lower Cr# of spinel from spinel lherzolites XM-3 and XM-9h indicate that they represent fertile mantle. In contrast, clinopyroxene from spinel lherzolite XM-1 has lower $Al_2O_3$ and HREE contents with LREE enrichment that can be attributed to refertilization by fluids/melts (e.g., Zhang et al. 2017). Enrichment of LREE and other LILE in clinopyroxene of sample XM-2 seems related with the reactions that formed the disequilibrium textures observed in this sample (Fig. 3d); this clinopyroxene could have been formed by reaction of a dunite with a melt with carbonatitic composition (e.g., Green and Wallace 1988). A high abundance of orthopyroxene, similar to sample XM-3, is often related to metasomatism by hydrous fluids and/or melts derived from a subducting slab, as interpreted in the subcratonic Kaapvaal mantle by several authors (e.g., Kesson and Ringwood 1989; Simon et al. 2007).

Calculated model melting curves based on the equations of Norman (1998) for the spinel stability field (Fig. 11) focused on the Y and Yb concentrations, since these two elements are less affected by metasomatic processes (e.g., Norman 1998; Zhang et al. 2017). Clinopyroxene is the main host of incompatible elements for these spinel lherzolites, and the composition of clinopyroxene from lherzolite XM-3 indicates up to 3% of melt extraction. The lower $Al_2O_3$ and HREE contents in the clinopyroxene from the spinel lherzolite XM-1 are indicative of a higher degree of melt extraction; this is also corroborated by the model curves (15% of batch or ~ 9% of fractional melting; Fig. 11).

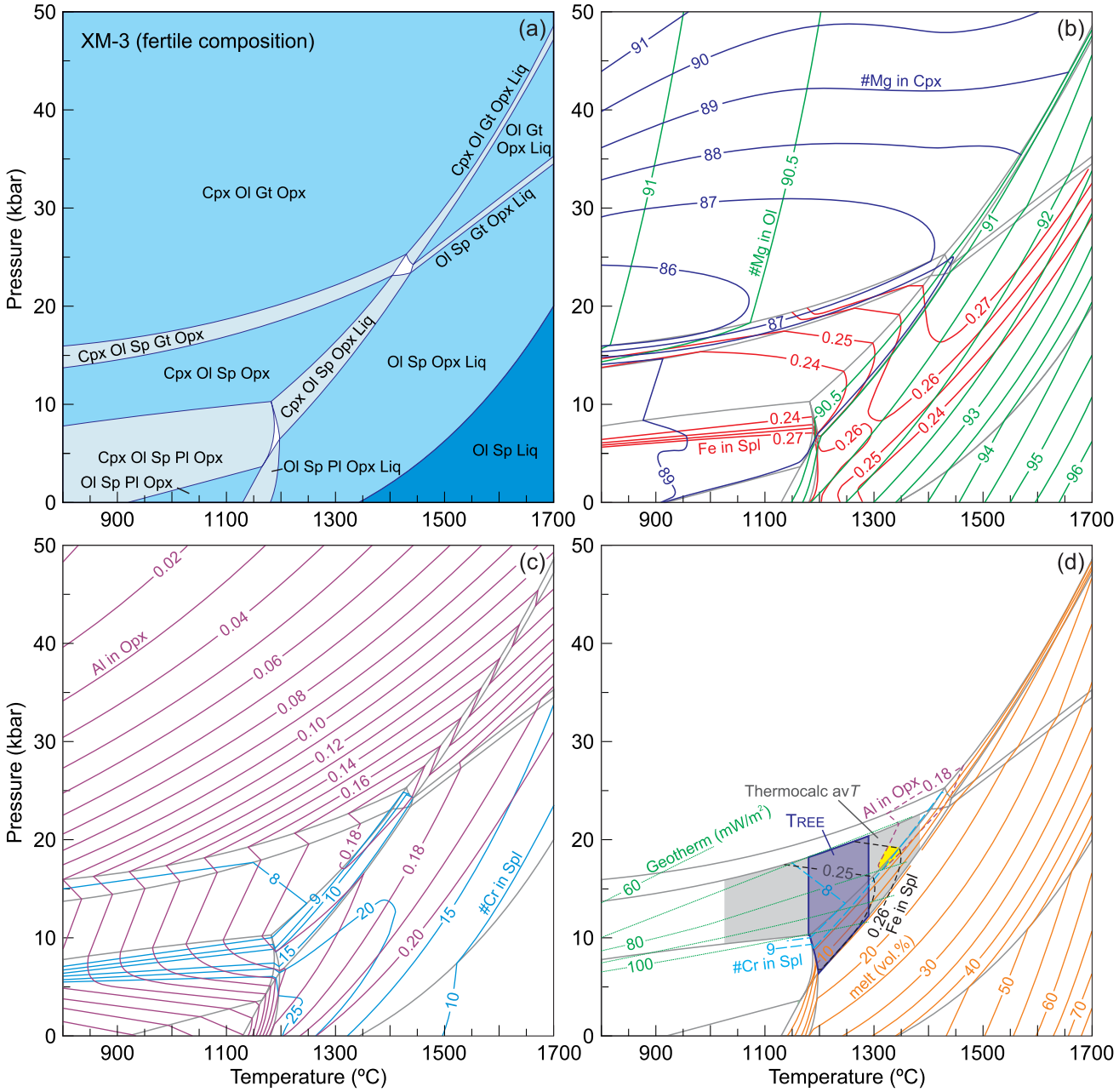


**Fig. 9** *P–T* isochemical phase diagrams calculated in the NCFMASOCr model system for fertile spinel lherzolite XM-3 (**a**), and compositional isopleths of Fe (apfu) and Mg# in olivine and clinopyroxene (**b**) and Cr# in spinel and Al (apfu) in orthopyroxene (**c**). Modeled compositions are indicated in Table 1. Also shown are modal isopleths of melt fraction. Dark-blue and gray fields in (**d**) represent thermometric results from REE-in-two-pyroxene thermometer ($T_{REE}$, Liang et al. 2013) and from average temperature (av*T*) Thermocalc calculations (Powell and Holland 1994), respectively. The yellow field corresponds to the best-fit peak *P–T* conditions estimated using intersections of compositional isopleths of Cr# and Fe in spinel and Al in orthopyroxene within the stability fields for mineral assemblages recognized in thin section. Geothermal gradients after Hasterok and Chapman (2011). Abbreviations for minerals are after Whitney and Evans (2010)

Figure 12 shows the chemical composition predicted for the primitive mantle after 1 and 12% of batch and 1, 3, and 5% of fractional melting. The HREE patterns of the spinel lherzolite samples overlap those produced by the Norman (1998) model calculations (Fig. 12). The negative HFSE anomalies (Nb, Ti, Zr and Hf) coupled with an enrichment of LILE (e.g., Sr), LREE, and Th (sample XM-1) are not observed in the model calculations. Sample XM-3 does not show a high LILE/HFS signature, as indicated, for instance, by a lower La/Nb (Fig. 5b). In contrast,

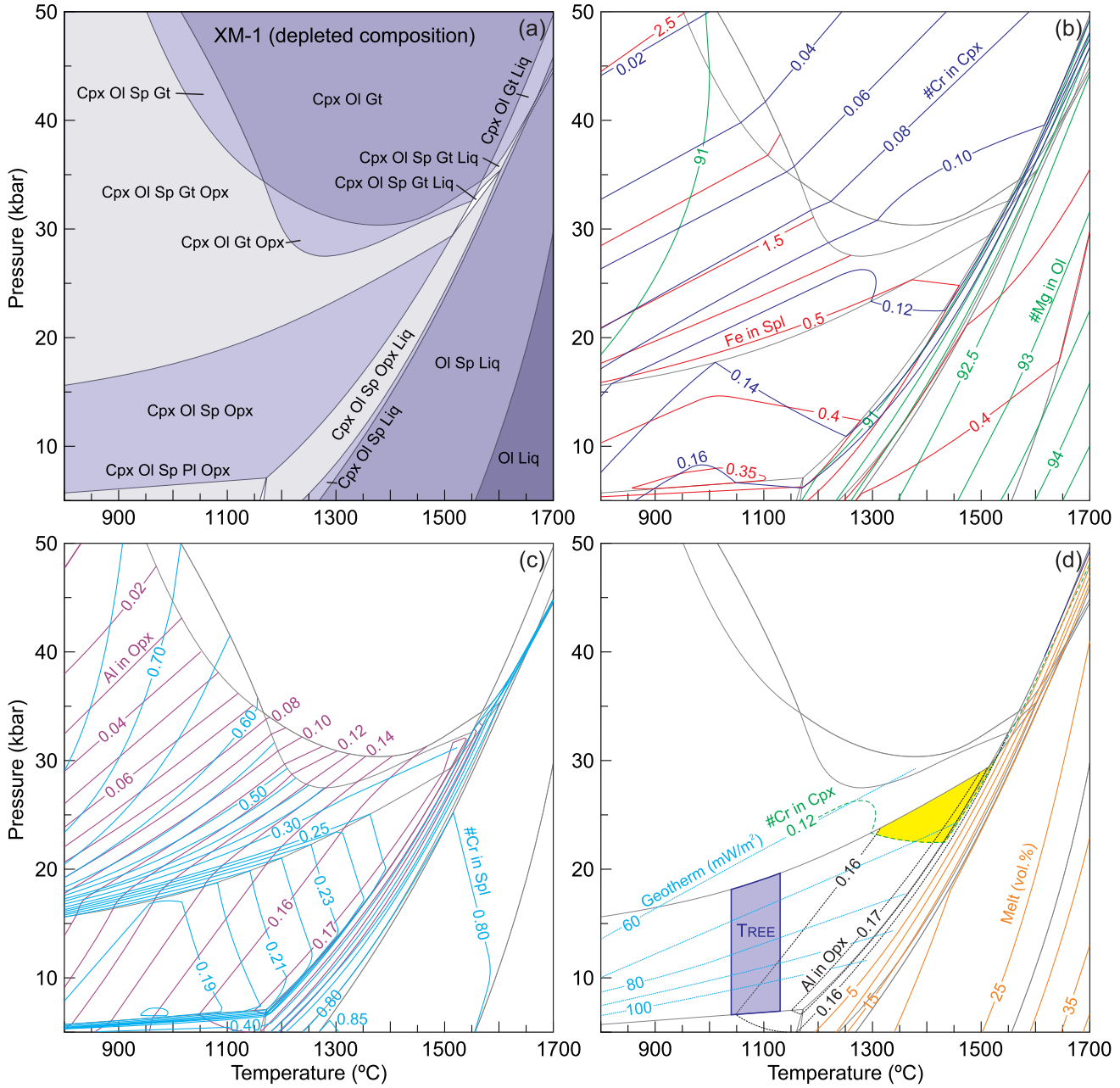


**Fig. 10** *P–T* isochemical phase diagrams calculated in the NCFMASOCr model system for the relatively depleted spinel lherzolite XM-1 (**a**), and compositional isopleths of Fe (apfu), Mg# in olivine and Cr# in clinopyroxene (**b**) and Cr# in spinel and Al (apfu) in orthopyroxene (**c**). Modeled compositions are indicated in Table 1. Also shown are modal isopleths of melt fraction (**d**). Dark-blue field in (**d**) represent thermometric results from REE-in-two-pyroxene thermometer (Liang et al. 2013).). The yellow field corresponds to the best-fit peak *P–T* conditions estimated using intersections of compositional isopleths of Cr# in clinopyroxene and Al in orthopyroxene within the stability field for mineral assemblage recognized in thin section. Geothermal gradients after Hasterok and Chapman (2011). Abbreviations for minerals after Whitney and Evans (2010)

clinopyroxene of sample XM-1 shows higher LILE/HFS (Fig. 5b) potentially linked with the nature of the metasomatic overprint constrained from this sample. Clinopyroxene from sample XM-2 was not considered in the model calculations as it displays textural disequilibrium.

## Thermal evolution of the SCLM: evidence from isochemical diagrams and conventional thermometry

Modeled isochemical phase diagrams indicate equilibria

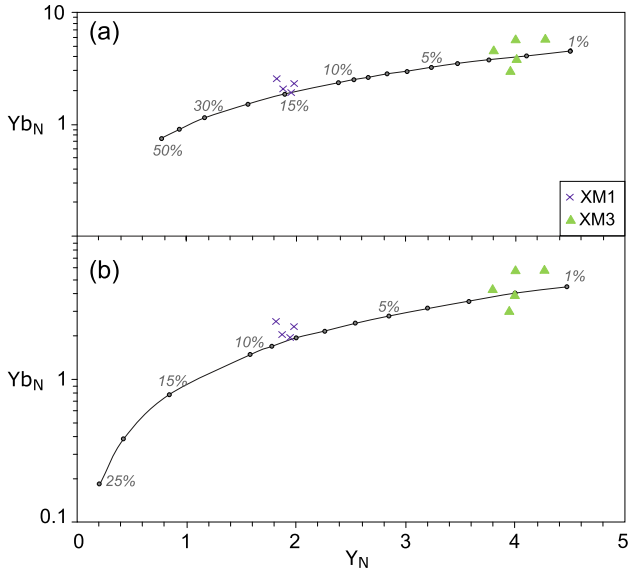


**Fig. 11** Modeling of batch (**a**) and fractional (**b**) melting using clinopyroxene compositions normalized to the primitive mantle (Sun and McDonough, 1989). The curves were constructed based on the equations presented in Norman (1998). The numbers referred to the proportion of partial melting

conditions of 1300–1350 °C and 17–19 kbar (sample XM-3; Fig. 9d) and 1300–1500 °C and 22–28 kbar (sample XM-1; Fig. 10d). Measured compositions for all minerals were well reproduced in the modeled diagram for sample XM-3, given robust peak *P*–*T* estimation from intersection of isopleths (Fig. 9d). In contrast, the spinel compositions were not reproduced in the modeled phase diagram for sample XM-1.

A comparison between the phase diagrams for samples XM-3 (more fertile, 2–3 vol% of melt extracted) and XM-1 (relatively depleted, 9–15 vol% of melt extracted) indicates that melt extraction has a great influence on the stability fields for the following assemblages: Cpx–Opx–Ol–Grt, Cpx–Opx–Ol–Grt–Spl, Opx–Ol–Spl–Liq, Cpx–Ol–Grt, Ol–Spl–Liq, and Ol–Liq, but a minor influence on the stability fields for spinel lherzolites (Fig. 9).

Temperature and pressure conditions estimated using the modeled isochemical phase diagrams are significantly higher than those commonly reported for spinel peridotite equilibria based on conventional thermobarometry (850–900 °C and 5–15 kbar; e.g., Wells 1977; Brey and Köehler 1990). Temperatures calculated with the thermometer of Brey and Köhler (1990) using average compositions of clinopyroxenes and orthopyroxenes are 807 °C for XM-3 and 755 °C for XM-1, assuming the pressure of 18 kbar (XM-3) and 20 kbar (XM-1) that correspond to the average pressure estimated in the isochemical diagrams. The application of the REE-in-two-pyroxene thermometer of Liang et al. (2013) gave values of 1233 ± 56 °C (XM-3) and 1085 ± 42 °C (XM-1). One possible explanation for these discrepant values is the difference in diffusion rates for divalent Mg and Fe in pyroxenes that are one to two order of magnitudes faster than diffusion rates for trivalent REE in pyroxenes (Liang et al. 2013). The average temperature of 1055 ± 178 °C obtained for sample XM-3 by multiequilibria thermometry is in agreement with the temperature interval obtained using the REE content.

The high temperatures (1300–1430 °C) estimated with calculated isochemical phase diagrams agree with data from thermodynamic models in the recent literature (Ziberna et al.

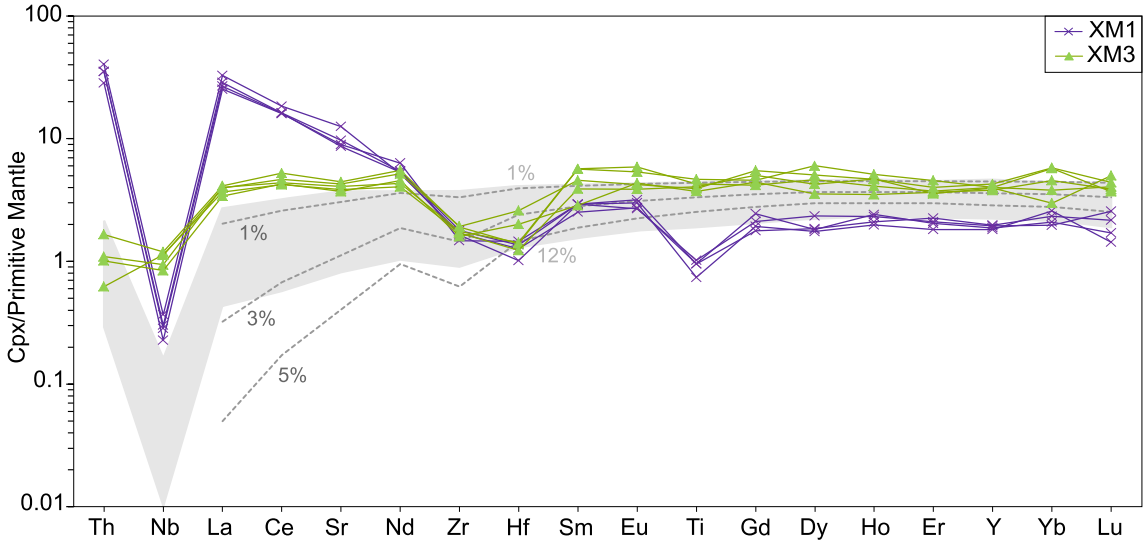


**Fig. 12** Multielement plots with the clinopyroxene compositions normalized to the primitive mantle of Sun and McDonough (1989). These are compared to the expected composition of the primitive mantle after 1% to 12% of batch melting (gray area) and 1, 3, and 5% of fractional melting (dashed points) based on the equations of Norman (1998)

2013; Jennings and Holland 2015; Jennings et al. 2016; Holland et al. 2018; Ziberna and Klemme 2016). Thermodynamic models applicable to melting of mantle rocks indicate that partial melting of plagioclase-free spinel peridotites occurs above 1150–1200 °C at 8–22 kbar (Green and Ringwood 1967; Jennings and Holland 2015; Jennings et al. 2016; Holland et al. 2018). The calculated phase diagrams reproduce very well the measured mineral compositions within the stability field of observed mineral assemblages (Fig. 9), and the predicted melt fraction modeled based on trace-element data in clinopyroxene (Fig. 11).

### Implications for the mantle evolution beneath the Ribeira Belt

The multiple methods used to constrain the *P–T* conditions (isochemical diagrams, $T_{REE}$) indicate that the lherzolites attained high temperatures (> 1200 °C), with high geothermal gradients of 65–80 mW/m$^2$, and experienced later re-equilibration (~ 800 °C). The observed difference between $T_{REE}$ and $T_{BKN}$ (˃100 °C) is expected for unstable thermal environments, such as those impacted by upwelling, hot asthenospheric mantle that interacted with cold, ancient, lithospheric mantle (Wang et al. 2015; Guo et al. 2017). The geothermal gradients are warmer than those constrained from mantle xenoliths enclosed in kimberlites located at the Brasília Belt, near the southwestern margin of the São Francisco Craton (e.g., Leonardos et al. 1993; Costa et al. 2008; Nannini 2016; Coldebella et al. 2020; Fernandes et al. 2021). The garnet peridotites of that region are equilibrated in a colder geotherm relative to spinel peridotites (35–40 vs. 40–50 mW/m$^2$) (e.g., Cabral Neto et al. 2017; Fernandes et al. 2021). The geothermal gradients calculated from mantle xenoliths of the Amazonian Craton are in the same range (38–45 mW/m$^2$) (Hunt et al. 2009; Costa 2016).

The Pb isotope ratios for clinopyroxene of sample XM-1 define an array that intercepts the Stacey-Kramers two-stage terrestrial Pb evolution curve at ca. 200 Ma. The array is most likely the result of mixing between subcontinental mantle and a younger metasomatic agent, which may be related to the host alkaline magma with Pb isotopic composition similar to the host lamprophyre dike (Garda 1995), alkaline dikes of the Serra do Mar region (Azzone et al. 2020), and Group I kimberlites (Smith 1983). The composition of the clinopyroxene for this sample (REE patterns, Pb isotopes) shows evidence that the mineral may have had a primary mantle origin overprinted by metasomatism from the Mesozoic alkaline melts. The *P–T* conditions with elevated temperatures and the time of reaction with the metasomatic agents possibly caused fast Pb diffusion in clinopyroxene (Cherniak 2001; Smart et al. 2017). The $^{238}U/^{206}Pb$ isochron ages are also suggestive of an overprint of the younger tectono-thermal event, most likely related to the opening and evolution of the South Atlantic Ocean, over a mantle previously equilibrated during the Precambrian development of the Ribeira Belt (571 ± 99 Ma).

## Conclusions

The spinel-facies peridotite samples examined here are hosted by a Cretaceous lamprophyre dike and represent fragments of the SCLM beneath the Ribeira Belt in southeastern Brazil. The olivine, pyroxene, and spinel compositions support the presence of a fertile mantle, and are consistent with low proportion of melt extraction and depletion of basaltic components (2–9% of fractional melting). Pressure and temperature estimates based on modeled isochemical phase diagrams of lherzolite samples vary from 1300–1350 °C and 17–19 kbar (fertile composition) to 1330–1430 °C and 17–23 kbar (relatively depleted composition); these correspond to high geothermal gradients of 65–80 mW/m$^2$. The temperature estimates based on the average REE contents of clinopyroxene vary from 1233 ± 56 °C to 1085 ± 42 °C, while conventional thermometry, based on the Fe–Mg exchange, suggests heterogeneous, lower re-equilibration temperatures (807 and 755 °C). The geothermal gradients are warmer than those constrained from mantle xenoliths located at the Brasília Belt, near the southwestern margin of the São Francisco Craton, and from the Amazonian cratonic root.

The Pb isotope ratios of clinopyroxene most likely represent a mixing line that intercepts the Stacey-Kramers two-stage terrestrial Pb evolution curve at ca. 200 Ma. The $^{238}U/^{206}Pb$ isochron yield ages of 56 ± 75 Ma and 571 ± 99 Ma. The older date suggests the presence of Precambrian mantle beneath the Ribeira Belt. The younger calculated Pb–Pb isotope errorchron age for spinel peridotite XM-1 most likely represents the influence of the Mesozoic magmatic event in the SCLM related with the opening and development of South Atlantic Ocean.

**Supplementary Information** The online version contains supplementary material available at https://doi.org/10.1007/s00531-022-02171-8.

**Acknowledgements** The present study was financially supported by Grants 2006/01925-4, 2007/00635-5, 2018/10012-0, and 2019/22084-8, São Paulo Research Foundation (FAPESP). VAJ, FMF, and RM thank the research productivity scholarship Grants 306102/2019-6, 307732/2019-3, and 305720/2020-1, respectively, and National Council of Technological and Scientific Development (CNPq). We thank Maria Irene Bartolomeu Raposo for the whole-rock compositional data of the lamprophyre dike. The paper was substantially improved following detailed comments and suggestions by Katie Smart and Gerhard Peter Brey. We thank Editor Wolf-Christian Dullo for his guidance during the editorial process.

**Author's contributions** VVA—conceptualization, methodology, investigation, and writing; VAJ—conceptualization, methodology, investigation, and writing; FMF—conceptualization, methodology, investigation, and writing; AS—methodology, investigation, and writing; RM—investigation and writing.

**Funding** The present study was financially supported by Grants 2006/01925–4, 2007/00635–5, 2018/10012–0, and 2019/22084–8, São Paulo Research Foundation (FAPESP).

## Declarations

**Conflict of interest** The authors declare no competing interests.

**Availability of data and materials** The results of mineral electron microprobe analyses, trace elements in minerals by LA-ICP-MS, and Pb isotopes in clinopyroxene are available in this article and in its Supplementary file.

**Code availability** Not applicable.

## References

Almeida VV, Janasi VA, Svisero DP, Nannini F (2014) Mathiasite-loveringite and priderite in mantle xenoliths from the Alto Paranaíba Igneous Province, Brazil: genesis and constraints on mantle metasomatism. Cent Eur J Geosci 6:614–632

Almeida VV, Janasi VA, Heaman LM, Shaulis B, Hollanda MHBM, Renne PR (2018) Contemporaneous alkaline and tholeiitic magmatism in the Ponta Grossa Arch, Paraná-Etendeka Magmatic Province: constraints from precise U–Pb zircon/baddeleyite and $^{40}Ar/^{39}Ar$ phlogopite dating of the José Fernandes Gabbro and mafic dykes. J Volcanol Geoth Res 355:55–65

Andrade S, Ulbrich HH, Gomes CB, Martins L (2014) Methodology for the determination of trace and minor elements in minerals and fused rock glasses with laser ablation associated with quadrupole inductively coupled plasma mass spectrometry (LA-Q-ICPMS). Am J Anal Chem 05:701–721

Assumpção M, Guarido M, van der Lee S, Dourado JC (2011) Upper-mantle seismic anisotropy from SKS splitting in the South American stable platform: a test of astenospheric flow models beneath the lithosphere. Lithosphere 3:173–180

Azzone RG, Munoz PM, Enrich GER, Alves A, Ruberti E, Gomes CB (2016) Petrographic, geochemical and isotopic evidence of crustal assimilation processes in the Ponte Nova alkaline mafic-ultramafic massif, SE Brazil. Lithos 260:58–75

Azzone RG, Ruberti E, Silva JCL, Gomes CB, Rojas GEE, Hollanda MHBM, Tassinari CCG (2018) Upper Cretaceous weakly to strongly silica-undersaturated alkaline dike series of the Mantiqueira Range, Serra do Mar alkaline province: Crustal assimilation processes and mantle source signatures. Br J Geol 48:373–390

Azzone RG, Chmyz L, Guarino V, Alves A, Gomes CB, Ruberti E (2020) Isotopic clues tracking the open-system evolution of the Ponte Nova mafic-ultramafic alkaline massif, SE Brazil: the contribution of Pb isotopes. Geochemistry 80:125648.

Baker J, Peate D, Waight T, Meyzen C (2004) Pb isotopic analysis of standards and samples using a 207Pb–204Pb double spike and thallium to correct for mass bias with a double-focusing MC-ICP-MS. Chem Geol 211:275–303

Bastin GF, van Loo FJJ, Heijiligers HJM (1984) Evaluation and use of Gaussian (Φ(pz)) curves in quantitative electron probe microanalysis: a new optimization. X-Ray Spectrom 13:91–97

Bastow ID, Julia J, do Nascimento A, Fuck R, Buckthorp T, Mc-Clellan J, (2015) Upper mantle anisotropy of the Borborema Province, NE Brazil: implications for intra-plate deformation and sub-cratonic asthenospheric flow. Tectonophysics 657:81–93

Beccaluva L, Bianchini G, Natali C, Siena F (2019) Plume-related Paraná-Etendeka Igneous Province: An evolution from plateau to continental rifting and breakup. Lithos 362–363:105484.

Bellieni G, Montes-Lauar CR, De Min A, Piccirillo EM, Cavazzini G, Melfi AJ, Pacca IG (1990) Early and Late Cretaceous magmatism from São Sebastião island (SE-Brazil): geochemistry and petrology. Geochim Br 4:59–83

Brey GP, Koehler T (1990) Geothermobarometry in four-phase lherzolites II: New thermobarometers and practical assessment of existing thermobarometers. J Petrol 31:1353–1378

Brito Neves BB, Campos Neto MC, Fuck RA (1999) From Rodinia to Western Gondwana: an approach to the Brasiliano-Pan African Cycle and orogenic collage. Episodes 22:155–166

Brotzu P, Melluso L, D'Amelio F, Lustrino M (2005) Potassic dykes and intrusions of the Serra do Mar Igneous Province (SE Brazil). In: Comin-Chiaramonti P, Gomes CB (eds) Mesozoic to Cenozoic Alkaline Magmatism in the Brazillian Platform. Edusp-Fapesp, pp 443–472

Cabral Neto I, Nannini F, Silveira FV, Cunha LM (2017) Áreas kimberlíticas e diamantíferas do Estado de Minas Gerais: Informe de Recursos Minerais Complementar ao Mapa das Áreas Kimberlíticas e Diamantíferas do Estado de Minas Gerais e Regiões Adjacentes. Brasília, Serviço Geológico do Brasil, 230 p.

Campanha GAC, Basei MAS, Tassinari C, Nutman AP, Faleiros FM (2008) Constraining the age of Iporanga Formation with SHRIMP U-Pb zircon: implications for possible Ediacaran glaciation in the Ribeira Belt, SE Brazil. Gondwana Res 13:117–125

Campanha GAC, Faleiros FM, Basei MAS, Tassinari CCG, Nutman AP, Vasconcelos PM (2015) Geochemistry and age of mafic rocks from the Votuverava Group, southern Ribeira Belt, Brazil: evidence for 1490 Ma oceanic back-arc magmatism. Precambrian Res 266:530–550

Campanha GAC, Basei MAS, Faleiros FM, Nutman AP (2016) The Mesoproterozoic to Early Neoproterozoic passive margin Lajeado Group and Apiaí Gabbro, southeastern Brazil. Geosci Front 7:683–694

Campanha GAC, Faleiros FM, Cawood PA, Cabrita DIG, Ribeiro BV, Basei MAS (2019) The Tonian Embu Complex in the Ribeira Belt (Brazil): revision, depositional age and setting in Rodinia and West Gondwana. Precambrian Res 320:31–45

Canil D, O'Neill HStC, Pearson DG, Rudnick RL, McDonough WF, Carswell DA, (1994) Ferric iron in peridotites and mantle oxidation states. Earth Planet Sci Lett 123:205–220

Carlson RW, Araújo ALN, Junqueira-Brod TC, Gaspar JC, Brod JA, Petrinovic IA, Hollanda MHBM, Pimentel MM, Sichel S (2007) Chemical and isotopic relationships between peridotites xenoliths and mafic-ultrapotassic rocks from Southern Brazil. Chem Geol 242(3–4):415–434

Carmichael ISE (1967) The iron-titanium oxides of salic volcanic rocks and their associated ferromagnesian silicates. Contrib Mineral Petr 14:36–64

Chen W, Simonetti A (2015) Isotopic (Pb, Sr, Nd, C, O) evidence for plume-related sampling of an ancient depleted mantle reservoir. Lithos 216–217:81–92

Cheng Z, Hou T, Keiding JK, Veksler IV, Kamenetsky VS, Hornschu M, Trumbull RB (2020) Comparative geothermometry in high-Mg magmas from the Etendeka Province and constraints on their mantle source. J Petrol 60(12):2509–2528

Cherniak DJ (1998) Pb diffusion in clinopyroxene. Chem Geol 150(1–2):105–117

Cherniak DJ (2001) Pb diffusion in Cr diopside, augite, and enstatite, and consideration of the dependence of cation diffusion in pyroxene on oxygen fugacity. Chem Geol 177:381–397

Chmyz L, Arnaud N, Biondi JC, Azzone RG, Bosch D (2019) Hf-Pb isotope and trace element constraints on the origin of the Jacupiranga Complex (Brazil): Insights into carbonatite genesis and multi-stage metasomatism of the lithospheric mantle. Gondwana Res 71:16–27

Coldebella B, Azzone RG, Chmyz L, Ruberti E, Svisero DP (2020) Oxygen fugacity of Alto Paranaíba kimberlites and diamond instability: Três Ranchos IV and Limeira I intrusions. Br J Geol 50(1):e20190087

Coltice N, Bertrand H, Rey P, Jourdan F, Phillips BR, Ricard Y (2009) Global warming of the mantle beneath continents back to the Archean. Gondwana Res 15:254–266

Connolly JA (2005) Computation of phase equilibria by linear programming: a tool for geodynamic modeling and its application to subduction zone decarbonation. Earth Planet Sci Lett 236:524–541

Costa GV, Gaspar JC, Moraes R, Coelho-Silva ATM, Carreiro S (2008) Mantle xenoliths from Canastra-01 kimberlite, Brazil. In: 9th International Kimberlite Conference. Extended Abstract No. 9IKC-A-00330

Costa VS (2016) Mineralogia e petrologia de xenólitos mantélicos da província kimberlítica de Juína, MT. PhD thesis, Instituto de Geociências, Universidade de São Paulo

Cury LF, Kaulfuss GA, Siga Junior O, Basei MAS, Harara OMM, Sato K (2002) Idades U-Pb (zircões) de 1.75 Ga em granitóides alcalinos deformados dos núcleos Betara e Tigre: evidências de regimes extensionais do Estateriano na Faixa Apiaí. Geologia USP, Série Científica, São Paulo v2:95–108

Deckart K, Féraud G, Marques LS, Bertrand H (1998) New time constraints on dyke swarms related to the Paraná-Etendeka magmatic province, and subsequent South Atlantic opening, southeastern Brazil. J Volcanol Geoth Res 80(1–2):67–83

Faleiros FM, Campanha GAC, Martins L, Valch SRF (2011) Ediacaran high-pressure collision metamorphism and tectonics of the southern Ribeira Belt (SE Brazil): Evidence for terrane accretion and dispersion during Gondwana assembly. Precambrian Res 189(3–4):263–291

Faleiros FM, Campanha GAC, Silva MP, Almeida VV, Rodrigues SWO, Araújo BP (2016) Short-lived polyphase deformation during crustal thickening and exhumation of a collisional orogeny (Ribeira Belt, Brazil). J Struct Geol 93:106–130

Felgate MR (2014) The petrogenesis of Brazilian kimberlites and kamafugites intruded along the 125º lineament: improved geochemical and geochronological constraints on magmatism in Rondonia and the Alto Paranaiba Igneous Province. PhD thesis, School of Earth Sciences, The University of Melbourne

Fernandes PR, Tommasi A, Vauchez A, Neves SP, Nannini F (2021) The São Francisco cratonic root beneath the Neoproterozoic Brasilia belt (Brazil): Petrophysical data from the kimberlite xenoliths. Tectonophysics 816:229011

Garda GM (1995) Os diques básicos e ultrabásicos da região costeira entre as cidades de São Sebastião e Ubatuba, estado de São Paulo. Instituto de Geociências, Universidade de São Paulo, Tese de doutorado

Garda GM, Schorscher HD, Esperança S, Carlson RW (1995) The petrology and geochemistry of coastal dikes from São Paulo State, Brazil: implications for variable lithospheric contributions to alkaline magmas from the western margin of the South Atlantic. An Acad Bras Cienc 67:191–216

Gomes CB, Ruberti E, Comin-Chiaramonti P, Azzone RG (2011) Alkaline magmatism in the Ponta Grossa Arch, SE Brazil: a review. J S Am Earth Sci 32:152–168

Green DH, Ringwood AE (1967) The stability fields of aluminous pyroxene peridotite and garnet peridotite and their relevance in upper mantle structure. Earth Planet Sci Lett 3:151–160

Green DH, Wallace ME (1988) Mantle metasomatism by ephemeral carbonatite melts. Nature 336:459–462

Griffin WL, O'Reilly SY, Afonso JC, Begg GC (2009) The composition and evolution of lithospheric mantle: a re-evaluation and its tectonic implications. J Petrol 50:1185–1204

Griffin WL, Powell WJ, Pearson NJ, O'Reilly SY (2008) Glitter: Data reduction software for laser ablation ICP-MS. In: Sylvester, P.J. (ed) Laser Ablation ICP-MS in the Earth Sciences: Current Practices and Outstanding Issues. Mineralogical Association of Canada Short Course Series. Short Course 40. Vancouver, pp. 308–311

Guo P, Xu W-L, Wang C-G, Wang F, Ge W-C, Sorokin AA, Wang Z-W (2017) Age and evolution of the lithospheric mantle beneath the Khanka Massif: Geochemical and Re-Os isotopic evidence from Sviyagino mantle xenoliths. Lithos 282–283:326–338

Hasterok D, Chapman DS (2011) Heat production and geotherms for the continental lithosphere. Earth Planet Sci Lett 307:59–70

Heaman L, Teixeira NA, Gobbo L, Gaspar JC (1998) U-Pb mantle zircon ages for kimberlites from the Juína and Paranatinga provinces. Brazil International Kimberlite Conference: Extended Abstracts 7(1):322–324

Heilbron M, Valeriano CM (2020) Comments on Meira VT, Garcia-Casco A, Hyppolito T, Juliani C, Schorscher JHD (2019) Tectono metamorphic evolution of the Central Ribeira Belt, Brazil: a case of Late Neoproterozoic intracontinental orogeny and flow of partially molten deep crust during the assembly of West Gondwana. Tectonics 39:e2019TC005897

Heilbron M., Soares ACP, Campos Neto M, Silva LC, Trouw R, Janasi VA (2004) Província Mantiqueira. In: Mantesso-Neto V, Bartorelli A, Carneiro CDR, Brito Neves BB (org). Geologia do Continente Sul Americano: Evolução da Obra de Fernando Flávio Marques de Almeida, 1st edn. São Paulo: Beca Produções Culturais Ltda., I:203–234

Heilbron M, Ribeiro A, Valeriano CM, Paciullo F, Almeida JCH, Trouw R, Tupinambá M, Silva LGE (2017) The Ribeira Belt. In: Heilbron M, Cordani U, Alkimim FF (org). São Francisco Craton, Eastern Brazil Tectonic Genealogy of a Miniature Continent, 1st edn. Springer, 1:277–304

Heilbron M, Valeriano CM, Peixoto C, Tupinambá M, Neubauer F, Dussin I, Corrales F, Bruno H, Lobato M, Almeida JCH, Silva LGE (2020) Neoproterozoic magmatic arc systems of the central Ribeira Belt, SE Brazil, in the context of the West Gondwana pre-collisional history: a review. J S Am Earth Sci 103:102710

Hellebrand E, Snow JE, Mostefaoui HP (2005) Trace element distribution between orthopyroxene and clinopyroxene in peridotites from the Gakkel Ridge: a SIMS and NanoSIMS study. Contrib Mineral Petrol 150:486–504

Henrique-Pinto R, Janasi VA, Vasconcellos ACBC, Sawyer EW, Barnes SJ, Basei MAS, Tassinari CCG (2015) Zircon provenance in meta-sandstones of the São Roque Domain: implications for the Proterozoic evolution of the Ribeira Belt, SE Brazil. Precambrian Res 256:271–288

Heron PJ (2018) Mantle plumes and mantle dynamics in the Wilson cycle. Geological Society, London, Special Publications 470(1):87–103

Holland TJB, Powell R (2011) An improved and extended internally consistent thermodynamic dataset for phases of petrological interest, involving a new equation of state for solids. J Metamorph Geol 29:333–383

Holland TJB, Green ECR, Powell R (2018) Melting of peridotites through to granites: a simple thermodynamic model in the system KNCFMASHTOCr. J Petrol 59:881–900. https://doi.org/10.1093/petrology/egy048

Hunt L, Stachel T, Morton R, Grütter H, Creaser RA (2009) The Carolina kimberlite, Brazil – Insights into an unconventional diamond deposit. Lithos 112(2):843–851

Hunt L, Stachel T, Grütter H, Armstrong J, McCandless TE, Simonetti A, Tappe S (2012) Small mantle fragments from the Renard kimberlites, Quebec: Powerful recorders of mantle lithosphere formation and modification beneath the Eastern Superior Craton. J Petrol 53(8):1597–1635

Jacob DE, Foley SF (1999) Evidence for Archean ocean crust with low high field strength element signature from diamondiferous eclogite xenoliths. Lithos 48:317–336

Janasi VA, Leite RJ, Van Schmus WR (2001) U-Pb ages and chronostratigraphy of the granitic magmatism in the Agudos Grandes batholith (W of Sao Paulo, Brazil)- implications for the evolution of the Ribeira Belt. J S Am Earth Sci 14(4):363–376

Janasi VA, Freitas VA, Heaman LH (2011) The onset of flood basalt volcanism, Northern Paraná Basin, Brazil: A precise U Pb baddeleyite/zircon age for a Chapecó-type dacite. Earth Planet Sci Lett 302:147–153

Jennings ES, Holland TJB (2015) A simple thermodynamic model for melting of peridotite in the system NCFMASOCr. J Petrol 56:869–892

Jennings ES, Holland TJB, Shorttle O, Maclennan J, Gibson SA (2016) The composition of melts from a heterogeneous mantle and the origin of ferropicrite: application of a thermodynamic model. J Petrol 57:2289–2310

Kaminsky FV, Sablukov SM, Belousova EA, Andreazza P, Tremblay M, Griffin WL (2010) Kimberlitic sources of super-deep diamonds in the Juina area, Mato Grosso State, Brazil. Lithos 114:16–29

Kesson SE, Ringwood AE (1989) Slab-mantle interactions: 2. The formation of diamonds. Chem Geol 78(2), 97–118.Lamotte DF, Fourdan B, Leleu S, Leparmentier F, Clarens P (2015) Style of rifting and the stages of Pangea breakup. Tectonics 34:1009–1029

Leonardos OH, Carvalho JB, Tallarico FHB, Gibson SA, Thompson RN, Meyer HOA, Dickin AP (1993) O xenólito de granada Iherzolito de Três Ranchos 4: uma rocha matriz do diamante na província magmática cretacea do Alto Paranaíba. In: I Simpósio de Geologia do Diamante, 1, Cuiabá. Annals, p. 3–16

Liang Y, Sun C, Yao L (2013) A REE-in-two-pyroxene thermometer for mafic and ultramafic rocks. Geochim Cosmochim Acta 102:246–260

Liu S, Tommasi A, Vauchez A, Mazzucchelli M (2019) Crust-mantle coupling during continental convergence and break-up: constraints from peridotite xenoliths from the Borborema Province, northeast Brazil. Tectonophysics 766:249–269

McDonough WF, Sun S-s (1995) The composition of the Earth. Chem Geol 120:223–253

Meira VT, García-Casco A, Juliani C, Almeida RP, Schorscher JHD (2015) The role of intracontinental deformation in supercontinent assembly: insights from the Ribeira Belt, southeastern Brazil (Neoproterozoic West Gondwana). Terra Nova 27(3):206–217

Mercier J (1980) Single-pyroxene thermobarometry. Tectonophysics 70:1–37

Nannini F (2016) Geologia e petrologia de xenólitos mantélicos da Província Ígnea do Alto Paranaíba, Minas Gerais. PhD thesis, Instituto de Geociências, Universidade de São Paulo

Ngonge ED, Hollanda MHBM, Pimentel MM, Oliveira DC (2016) Petrogenesis of the alkaline rocks of the Macau volcanic field, NE Brazil. Lithos 266–267:453–470

Ngonge ED, Hollanda MHBM, Puchtel IS, Walker RJ, Archanjo CJ (2019) Characteristics of the lithospheric mantle beneath northeastern Borborema Province, Brazil: Re-Os and HSE constraints on peridotite xenoliths. J S Am Earth Sci 96:102371

Norman MD (1998) Melting and metasomatism in the continental lithosphere: laser ablation ICPMS analysis of minerals in spinel lherzolites from eastern Australia. Contrib Mineral Petrol 130:240–255

Palin RM, Weller OM, Waters DJ, Dyck B (2016) Quantifying geological uncertainty in metamorphic phase equilibria modelling; a Monte Carlo assessment and implications for tectonic interpretations. Geosci Front 7(4):591–607

Pearson DG, Canil D, Shirey SB (2014) 3.5 — mantle samples included in volcanic rocks: xenoliths and diamonds. In: Holland HD, Turekian KK (eds). Treatise on Geochemistry Elsevier, 2nd edn. Oxford,169–253

Powell R, Holland TJB (1994) Optimal Geothermometry and Geobarometry Am Mineral 79:120–133

Raposo MIB (2017) Magnetic fabrics of the Cretaceous dike swarms from São Paulo coastline (SE Brazil): Its relationship with South Atlantic Ocean opening. Tectonophysics 721:395–414

Regelous M (1993) Geochemistry of dolerites from the Paraná flood basalt province, southern Brazil. Unpublished PhD thesis, Open University

Ricardo BS. Faleiros FM, Moraes R, Siga Junior O, Campanha GAC (2020) Tectonic implications of juxtaposed high- and low-pressure metamorphic field gradient rocks in the Turvo-Cajati Formation, Curitiba Terrane, Ribeira Belt, Brazil. Precambrian Res 345:105766

Rivalenti G, Mazzucchelli M, Girardi VAV, Vannucci R, Barbieri MA, Zanetti A, Goldstein SL (2000) Composition and processes of the mantle lithosphere in northeastern Brazil and Fernando de Noronha: evidence from mantle xenoliths. Contrib Mineral Petrol 138:308–325

Rocha MP, Schimmel M, Assumpção M (2011) Upper-mantle seismic structure beneath SE and Central Brazil from *P*- and *S*-wave regional traveltime tomography. Geophys J Int 184:268–286

Schmidberger SS, Simonetti A, Heaman LM, Creaser RA, Whiteford S (2007) Lu–Hf, in-situ Sr and Pb isotope and trace element systematics for mantle eclogites from the Diavik diamond mine: evidence for Paleoproterozoic subduction beneath the Slave craton, Canada. Earth Planet Sci Lett 254:55–68

Siga Junior O (1995) Domínios tectônicos do sudeste do Paraná e nordeste de Santa Catarina: geocronologia e evolução crustal. PhD thesis, Instituto de Geociências, Universidade de São Paulo. 212 p

Simakov S, Dolivo-Dobrovolsky M (2009) PTQuick. Versions 1.4.0.5 (PTQuick.exe), 1.4.0.12 (PTools.dll), http://dimadd.ru/en/Programs/ptquick

Simon NSC, Carlson RW, Pearson DG, Davies GR (2007) The origin and evolution of the Kaapvaal cratonic lithospheric mantle. J Petrol 48(3):589–625

Smart KA, Chacko T, Simonetti A, Sharp ZD, Heaman LM (2014) A record of paleoproterozoic subduction preserved in the Northern Slave Cratonic Mantle: Sr-Pb-O isotope and trace-element investigations of eclogite xenoliths from the Jericho and Muskox kimberlites. J Petrol 55:549–583

Smart KA, Tappe S, Simonetti A, Simonetti SS, Woodland AB, Harris C (2017) Tectonic significance and redox state of Paleoproterozoic eclogite and pyroxenite components in the Slave cratonic mantle lithosphere, Voyageur kimberlite, Arctic Canada. Chem Geol 455:98–119

Smith CB (1983) Pb, Sr and Nd isotopic evidence for sources of Southern African Cretaceous Kimberlites. Nature 304(5921):51–54

Stacey JS, Kramers JD (1975) Approximation of terrestrial lead isotope Evolution by a two-stage model. Earth Planet Sci Lett 26:207–221

Sun S-S, McDonough WF (1989) Chemical and isotopic systematics of oceanic basalts: implications for mantle composition and processes. In: Saunders AD, Norry MJ (eds) Magmatism in the ocean basins. Geological Society of London, London, 42:313–345

Tappe S, Smart KA, Pearson DG, Steenfelt A, Simonetti A (2011) Craton formation in Late Archean subduction zones revealed by first Greenland eclogites. Geology 39:1103–1106

Thompson RN, Gibson SA, Mitchell JG, Dickin AP, Leonardos OH, Brod JA, Greenwood JC (1998) Migrating Cretaceous-Eocene magmatism in the Serra do Mar Alkaline Province, SE Brazil: Melts from the deflected Trindade mantle plume? J Petrol 39:1493–1526

Tommasi A, Vauchez A (2015) Heterogeneity and anisotropy in the lithospheric mantle. Tectonophysics 661:11–37

Vauchez A, Tommasi A, Mainprice D (2012) Faults (shear zones) in the Earth´s mantle. Tectonophysics 558–559:1–27

Vicentini CM (2015) Caracterização geoquímica e isotópica (Sr-Nd-Pb) dos litotipos subalcalinos diferenciados do enxame da Serra do Mar. Instituto de Astronomia, Geofísica e Ciências Atmosféricas. Universidade de São Paulo, Dissertação de Mestrado, p 94

Wang C, Liang Y, Xu W (2015) On the significance of temperatures derived from major element and REE based two-pyroxene thermometers for mantle xenoliths from the North China Craton. Lithos 224–225:101–113

Wells PRA (1977) Pyroxene thermometry in simple and complex systems. Contrib Mineral Petr 62:129–139

Whitney DL, Evans BW (2010) Abbreviations for names of rock-forming minerals. Am Mineral 95:185–187. https://doi.org/10.2138/am.2010.3371

Zhang H, Zheng J, Pan S, Lu J, Li Y, Xiang L, Lin A (2017) Compositions and processes of lithospheric mantle beneath the west Cathaysia block, southeast China. Lithos 286–287:241–251

Ziberna L, Klemme S (2016) Application of thermodynamic modelling to natural mantle xenoliths: examples of density variations and pressure–temperature evolution of the lithospheric mantle. Contrib Mineral Petr 171:16

Ziberna L, Klemme S, Nimis P (2013) Garnet and spinel in fertile and depleted mantle: insights from thermodynamic modelling. Contrib Mineral Petr 166:411–421. https://doi.org/10.1007/s00410-013-0882-5